Variability of acoustically evidenced methane bubble emissions offshore western Svalbard

Mario E. Veloso-Alarcón[1,2], Pär Jansson[3], Marc De Batist[2], Timothy A. Minshull[4], Graham K. Westbrook[5], Heiko Pälike[4], Stefan Bünz[3], Ian Wright[6], Jens Greinert[1,2,3]

[1]GEOMAR Helmholtz Centre for Ocean Research Kiel, Wischhofstr. 1-3 24148 Kiel, Germany.
[2]Renard Centre of Marine Geology, Ghent University, Krijgslaan 281 s.8 B-9000 Ghent, Belgium.
[3]CAGE-Centre for Arctic Gas Hydrate, Environment and Climate, Department of Geosciences, UiT-The Arctic University of Norway, Postboks 6050 Langnes, N-9037 Tromsø, Norway.
[4]National Oceanography Centre Southampton, University of Southampton, European Way, Southampton SO14 3ZH, United Kingdom.
[5]School of Geography, Earth and Environmental Sciences, University of Birmingham, Edgbaston, United Kingdom.
[6]Vice-Chancellor's Office, University of Canterbury, Private Bag 4800, Christchurch, New Zealand.

Corresponding author: Mario E. Veloso-Alarcón (mveloso@geomar.de)

Key Points

- Hydroacoustically derived flow-rates from three areas offshore Svalbard range from 2900 to 4500 t CH_4 y^{-1}
- No clear trend of CH_4-bubble fluxes over time can be identified
- Alternating CH_4-bubble seepage between two areas suggests geological interconnectivity between them.
- No spatial migration of bubble-seepage over time at the landward limit of the hydrate stability zone was observed.

Abstract

Large reservoirs of methane present in Arctic marine sediments are susceptible to rapid warming, promoting increasing methane emissions. Gas bubbles in the water-column can be detected and flow-rates can be quantified using hydroacoustic survey methods, making it possible to monitor spatiotemporal variability. We present methane (CH_4) bubble flow-rates derived from hydroacoustic datasets acquired during 11 research expeditions to the western Svalbard continental margin (2008-2014). Three seepage areas emit in total 2900–4500 t CH_4 y^{-1} and bubble fluxes are up to 8 kg $m^{-2}yr^{-1}$. Bubble fluxes vary between different surveys but no clear trend can be identified. Flux variability analyses suggest that two areas are geologically interconnected, displaying alternating flow changes. No spatial migration of bubble-seepage over time at the landward limit of the hydrate stability zone was observed, suggesting that shallow hydrate dissociation is not significant enough to be observed by changes in bubble emissions.

1 Introduction

Underwater CH_4-bubble emissions were thought to contribute significantly to global climate change (Hornafius et al., 1999; Kvenvolden, 1993; Shakhova et al., 2010, 2014), but recent evidence has challenged this suggestion. Numerical bubble modeling has shown that, except in water depths shallower than ca. 100 m, CH_4 bubbles mostly dissolve (e.g., McGinnis et al., 2006; Vielstädte et al., 2015) and methane is oxidized before it reaches the atmosphere/ocean interface(Steinle et al., 2016). Additionally, CH_4 seepage has been postulated to contribute to ocean acidification (Biastoch et al., 2011; Pohlman et al., 2011) and deoxygenation (Boetius & Wenzhöfer, 2013; Yamamoto et al., 2014) . Arctic marine sediments sequester large quantities of CH_4 in natural gas deposits, submarine permafrost and gas hydrates (O'Connor et al., 2010; Shakhova et al., 2014). Mechanisms for CH_4 release from these reservoirs are poorly constrained but likely comprise hydrate dissociation (Westbrook et al., 2009), submarine permafrost thawing with increased anaerobic organic matter degradation due to ongoing bottom-water warming (James et al., 2016), or pressure decrease from deglaciation and sea-level change (Andreassen et al., 2017).

Sediments on the western Svalbard continental margin are influenced by the northward inflow of rapidly warming Atlantic water (AW). Therefore, gas hydrates, if present therein, are more susceptible to dissociation than elsewhere. West of Prins Karls Forland (PKF), a significant number of methane seeps were identified in 2008 (Westbrook et al., 2009) and this area received additional attention because the seepage was attributed to ocean-warming-induced hydrate destabilization (Berndt et al., 2014; Sahling et al., 2014). The area was investigated to reveal the gas origin (e.g., Gentz et al., 2014; Sahling et al., 2014), describe sub-seabed migration mechanisms (e.g., Mau et al., 2017; Rajan et al., 2012; Sarkar et al., 2012), determine the fate of gas released into the water-column (e.g., Graves et al., 2015; Steinle et al., 2015), evaluate the warming potential due to CH_4 transfer to the atmosphere (e.g., Fisher et al., 2011; Pisso et al., 2016; Pohlman et al., 2017), and in general elucidate a possible relationship between bubble-release and ocean warming (e.g., Berndt et al., 2014; Mau et al., 2017).

Acoustic flares, the hydroacoustic expression of underwater bubble release, were first detected in the area in 2008 (Westbrook et al., 2009) and hydroacoustic evidence of bubble-seepage has been reported repeatedly since then (Berndt et al., 2014; Lund Myhre et al., 2016; Sarkar et al., 2012; Veloso et al., 2015). Our study comprises single-beam echosounder (SBES) data collected during 11 surveys carried

out between 2008 and 2014 by R/V Helmer Hanssen (RVHH) and RRS James Clark Ross (RRSJCR). The data allow the first spatiotemporal variability analysis of submarine bubble seepage offshore PKF and its first quantitative comparison over several years using the hydroacoustic information.

The study area is located west of Svalbard at the shelf offshore PKF (Fig.1), where the distribution of flares shows three active sub-areas (Fig.1) that we name SBreak-Area (shelf-break, ~200 mbsl), Slope-Area (upper slope, 300-400 mbsl) and Shelf-Area (shelf, ~90 mbsl). Isotope analysis of gas collected at the seabed in SBreak-Area and Slope-Area ($\delta^{13}C_{CH4}$ = - 55.7 ‰; Mau et al., 2017; Sahling et al., 2014) and CH_4 in sea surface waters in Shelf-Area ($\delta^{13}C_{CH4}$ =−54.6‰, Pohlman et al., 2017) suggest a microbial methane origin. High-resolution seismic data in SBreak-Area and Slope-Area suggest that fluids migrate through vertical pathways from deeper hydrocarbon reservoirs and flow upslope along near-horizontal permeable layers (Rajan et al., 2012; Sarkar et al., 2012). It has been proposed that the main seepage locations are determined by sediment permeability at Slope-Area (Sarkar et al., 2012) and by the intersection with the seabed of the latest prograding glacigenic sequence at SBreak-Area (Rajan et al., 2012). Seepage at Slope-Area has been hypothesized to be a consequence of hydrate dissociation triggered by bottom-water warming because flares seem to be aligned with the landward limit of the gas hydrate stability zone (LGHZ) (Westbrook et al., 2009). So far, no hydrates have been recovered near SBreak-Area and no clear and widespread bottom-simulating reflector has been observed close to the bubbling area. However, negative-polarity seismic bright spots have been found at the base of the theoretical gas hydrate stability zone (GHSZ) in that area, so the presence of hydrates cannot be disregarded (Sarkar et al., 2012). Seepage at Shelf-Area has been attributed to hydrate dissociation triggered by ice-sheet unloading, with the present-day seepage locations marking previous GHSZ pinch-out locations (Portnov et al., 2016). This hypothesis is supported by similar evidence from the formerly glaciated continental margin of the Barents Sea (Andreassen et al., 2017). Earthquakes related to extension of the nearby spreading ridge system (Fig.1) may influence bubble-seepage indirectly (Plaza-Faverola et al., 2015).

Two ocean currents control the water properties in the area; the West Spitsbergen Current introduces warm and saline AW from the south; and the Coastal Current contributes fresher and colder Transformed Atlantic Water to the northward flow (Graves et al., 2015; Nilsen et al., 2016). Bottom-water temperature changes on seasonal to decadal timescales have been proposed to cause shallow hydrate formation and dissociation in Slope-Area, yielding a positive correlation between ocean temperature and bubble release (Berndt et al., 2014; Westbrook et al., 2009). However, the hydrate occurrence zone is expected to be thinner than the GHSZ because hydrate formation is limited by supply of water and CH_4 in excess of its solubility, and by anaerobic oxidation in the sulfate reduction zone (SRZ) (Ruppel & Kessler, 2017). Therefore, hydrates are unlikely to be present within a few meters of the seabed, where a seasonal heat-pulse could be transmitted, and bubble-seepage modulation associated with seasonal hydrate formation/dissociation is likely to be weak.

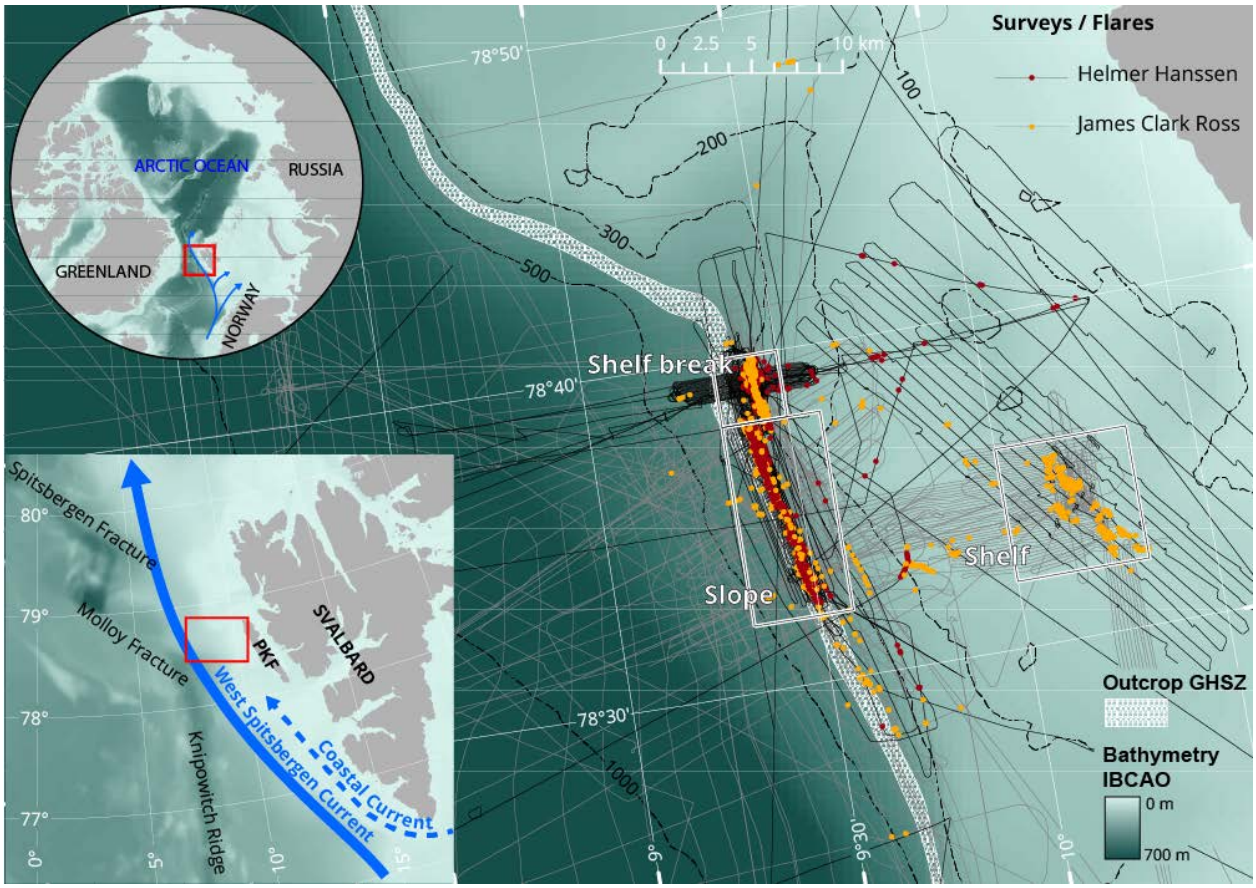

Figure 1. Bathymetric map of the study area. Black tracks with red flare locations mark RVHH surveys and grey tracks with yellow flare locations mark RRSJCR surveys. White hex pattern marks migration of the LGHZ (360-410 m isobaths; Westbrook et al., 2009). Rectangles indicate the survey areas.

2 Materials, Methods, and Results

2.1 Hydroacoustic detection of gas venting

We analyzed hydroacoustic water-column data from 11 surveys conducted during 2008–2014: S1 (08/2008); S2 (07/2009) S3 (10/2010); S4 (07/2011); S5 (08/2011); S6 (07/2012); S7 (07/2012); S8 (07/2013); S9 (10/2013); S10 (06/2014); S11 (10/2014); see supplementary information (SI); Table SI1. Data were acquired with an EK60 SBES (Kongsberg) and calibrated routinely, using moving spheres (Foote, 1987), allowing for unbiased comparison of absolute target-strength values (TS; logarithm of ratio between scattered and incident acoustic intensities; dB re 1 m^2). We used the 38 kHz frequency for this study because it is common between the two vessels and it presented the best backscattering response of bubbles, with the lowest signal-to-noise ratio at depths relevant to the study area (SI, Fig. SI1). We identified 3145 acoustic flares (SI, Fig. SI2) and selected those flares that could be traced clearly from the seabed and were well above the background noise (10 dB-TS above average background-noise of ~70 dB-TS). A representative TS of each flare in a layer 5-10 m above the seafloor was extracted with the FlareHunter graphical user interface (FH-GUI; http://www.geomar.de/en/research/fb2/fb2-mg/deepsea-monitoring/software/flarehunter-and-fluxmodule/) . The representative TS was calculated by averaging discrete TS values of the central pings within a flare and within the 5m thick layer above the seafloor. The georeferenced center of this virtual footprint was obtained by averaging the motion-compensated beam centers of the selected pings projected at the layer average depth. A virtual footprint-area was derived for this location and depth (SI, Text SI1).

Subsequently, CH_4 flow rates (amount per time unit) for individual flares were calculated, using the inverse hydroacoustic method embedded in the FH-GUI (Veloso et al., 2015). A bubble size distribution (BSD) derived from video observations conducted during cruises S2 and S3 (Veloso et al., 2015; SI, Fig. SI4), and various bubble rising speed models (BRSM's) for 'clean´ and ´dirty´ bubbles (Leifer et al., 2000, 2015; Leifer & Patro, 2002; Mendelson, 1967; Woolf, 1993; Woolf & Thorpe, 1991; SI, Fig. SI5; all included in FH-GUI) were used. Ambient water properties, gas, and environmental constants used for CH_4 flow rate quantification are specified in the SI (Table SI2).

2.2 Areal flow-rates

Areal flow-rates were calculated for the three areas by integrating the calculated flare flow-rates from all the surveys. Flares were clustered if their footprints overlapped, to avoid flow rate overestimations resulting from repeatedly insonified bubbling-sectors. Equivalent cluster fluxes were calculated by averaging the individual fluxes (flare flow-rates normalized by their respective virtual footprint-area) of flares within a cluster. A cluster flow-rate was derived by multiplying the equivalent cluster-flux by the cluster-area (Veloso et al., 2015; SI, Text SI4). Finally, areal flow rates were derived by summation of cluster flow-rates and isolated flare flow-rates (no overlap with other flares) for the three sub-areas (Table 1)

2.3 Flux through time

Each dataset results in a unique insonified area; even if tracks between surveys were identical, the insonified areas at the seafloor were not, due to vessel motion. Therefore, flow rates derived from different surveys cannot be compared directly as temporal analysis will have spatial bias. However, bubble fluxes (flow rates normalized by insonified areas) can be used for variability analysis. We developed a common area flux method (CAF; SI, Text SI5) based on the comparison of fluxes from bubbling areas that were repeatedly insonified during surveys (including clustered and isolated flares, and their respective flux values). The method follows the same technique described in section 2.2 but instead only flares from the same survey are clustered. The georeferenced flare and cluster areas were gridded creating a regular survey matrix with respective flux values for each cell. A common bubbling area between surveys was extracted from the survey matrices (SI, Fig. SI9) and a representative flux (Q_{RF}) was calculated, using the arithmetic mean of fluxes in the common area (Fig. 2). No grid cell was covered by all 11 surveys but small areas were covered by up to 8 surveys. Our analysis included multiple combinations of survey matrices with a minimum of two overlapping surveys for area SBreak-Area and Slope-Area (Fig. 1). Several Q_{RF} were obtained for each survey from the multiple combinations. The average of these values per survey ($\overline{Q}_{RF}$) is shown in Fig. 2. Shelf-Area was not considered in this analysis since it was only surveyed once. Since flux magnitudes and their changes are very similar when using different ‘clean’ and ‘dirty’ BRSMs, we only show the results for clean bubbles using the ‘Leifer’ rising speed model (Leifer et al., 2015).

Table 1. Volumetric and mass flow rates of CH4 calculated using merged hydroacoustic information of SBreak-Area, Slope-Area, and Shelf-Area using different BRSM's (SI, Figure SI5; M1C: "Leifer" clean; M2C: "Mendelson" clean; M3C: "Leifer & Patro" clean; M1D:"Leifer" clean; M2D: "Leifer & Patro" dirty; M3D: "Woolf93"; M4D: "Thorpe 91" dirty).

	Clean bubble models			Dirty bubble models			
A-SBreak	**M1C**	**M2C**	**M3C**	**M1D**	**M2D**	**M3D**	**M4D**
Flow-rate vol (L/min)	122.96	158.28	156.43	101.32	126.91	158.40	136.33
Flow-rate mass (T/yr)	1032.03	1328.57	1313.00	850.41	1065.19	1329.51	1144.31
Area with acoustic data [m^2]				646234			
Mean annual flow-rate [T/yr]		1224.53			1097.35		
Standard deviation flow-rate BRSM [T/yr]		166.89			198.42		
***Mean relative error flow-rate BRSM [%]**		± ~ 10			± ~ 12		
A-Slope	**M1C**	**M2C**	**M3C**	**M1D**	**M2D**	**M3D**	**M4D**
Flow-rate vol (L/min)	150.49	195.18	192.92	124.01	156.46	195.28	168.08
Flow-rate mass (T/yr)	1949.25	2528.28	2499.05	1606.23	2026.77	2529.69	2177.31
Area with acoustic data [m^2]				1466867			
Mean annual flow-rate [T/yr]		2325.53			2085.00		
Standard deviation flow-rate BRSM [T/yr]		326.19			382.48		
***Mean relative error flow-rate BRSM [%]**		± ~ 10			± ~ 12		
A-Shelf	**M1C**	**M2C**	**M3C**	**M1D**	**M2D**	**M3D**	**M4D**
Flow-rate vol (L/min)	60.80	78.53	77.62	50.10	62.96	78.58	67.64
Flow-rate mass (T/yr)	555.96	718.50	710.14	458.12	576.02	718.95	618.82
Area with acoustic data [m^2]				507447			
Mean annual flow-rate [T/yr]		661.53			592.98		
Standard deviation flow-rate BRSM [T/yr]		126.21			108.03		
***Mean relative error flow-rate BRSM [%]**		± ~ 10			± ~ 12		

*mean relative error (%) = $\frac{100}{N}\sum_{i=1}^{N}\frac{|x_i-\overline{x}|}{\overline{x}}$

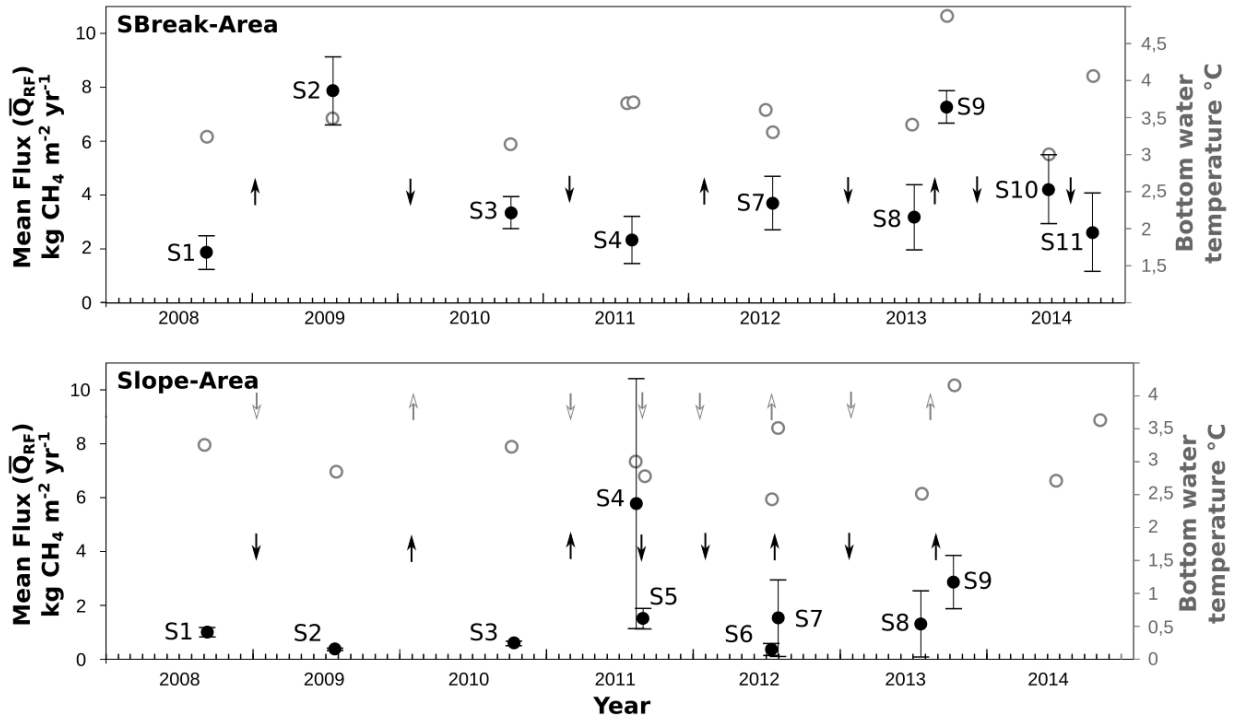

Figure 2. Temporal variability of CH_4-fluxes in SBreak-Area and Slope-Area derived with the CAF method using BRSM M1C. Black dots represent mean Q_{RF} fluxes; error bars show the standard deviation of fluxes from common areas used to calculate the mean Q_{RF} flux. Grey open dots represent the mean bottom-water temperatures (SI, Excel and Matlab files). Grey (open) and black arrows indicate changes in temperature and fluxes between surveys, respectively.

3 Discussion

3.1. Quantifying bubble-emissions

Assuming continuous release of pure CH4 bubbles, we estimate yearly emissions of ~850-1300, 1600-2500, and 450-700 tons for SBreak-Area, Slope-Area, and Shelf-Area, respectively. These results are comparable with other estimates for sub-areas of SBreak-Area and Slope-Area (Sahling et al., 2014), and are similar to comparable seepage areas elsewhere (Römer et al., 2014, 2012a, 2012b; Sauter et al., 2006; Schneider von Deimling et al., 2011; Torres et al., 2002; SI, Table SI5). Previously obtained flow rates from a sub-section of SBreak-Area using the same hydroacoustic method (Veloso et al., 2015) are half of the values presented here. This difference can be attributed to the difference in the area covered and its location. The risk of missing bubbling areas is reduced by increasing the SBES coverage, so the flow-rates derived from our larger dataset (merging of 9 surveys) represent better the bubble release for SBreak-Area (~ 850-1300 t CH4 yr^{-1} from ~13.4 km^2) than those determined by Veloso et al. (2015) using two surveys. Variations can also be introduced by inaccurate flare locations, which result in a flow rate overestimation if the same flare is considered multiple times. Transient bubble release creates another uncertainty since short-term variability is neglected when data from different surveys are combined.

A survey at PKF combining multibeam echosounder (MBES) and a ROV-based visual inspection (Sahling et al., 2014) suggested that 433 and 417 t CH_4 yr^{-1} are emitted from areas comparable to SBreak-Area and Slope-Area, respectively. This is 2.5 to 5 times lower than our results (1075 and 2050 t CH_4 yr^{-1}), but our estimate in sub-area SBreak-Area is within the uncertainty of that study. The difference can be attributed to uncertainties in both methods. While flow rates calculated from optical methods are more precise than those from SBES-data inversion, uncertainties arise when extrapolating flow rates from a few visual-observations to a larger number of MBES-detected flares. SBES-data inversion may decrease these uncertainties by using the backscatter heterogeneity of all detected flares to derive flow rates, but incorporates other uncertainties (e.g., from the backscattering model, BRSM's, and BSD observations; see Veloso et al., 2015). Future surveys should consider the combination of both methods to improve the flow rate assessment of large seepage areas.

3.2 Seepage variability

Our results show that CAF values in SBreak-Area vary between 2 and 8 kg CH_4 m^{-2} yr^{-1} with a standard deviation of 0.6-1.4 kg CH_4 $m^{-2}yr^{-1}$ (Fig. 2). This result indicates that common areas used to calculate a $\overline{Q}_{RF}$ during each survey have similar gas emissions. Fluxes fluctuate around a mean of 3 kg CH_4 $m^{-2}yr^{-1}$, except during S2 and S9, which exhibit higher fluxes (~7.8 and ~7.2 kg CH_4 yr^{-1} m^{-2}, respectively). In Slope-Area, fluxes range from 0.35 to 5.7 kg CH_4 yr^{-1} m^{-2} with a mean of 1.7 kg CH_4 yr^{-1} m^{-2}. A peak flux is observed for survey S4, with a standard deviation of ~4.68 kg CH_4 yr^{-1} m^{-2}, which is perhaps high due to spatial separation of the common areas involved in the mean Q_{RF} calculation. All other $\overline{Q}_{RF}$ values exhibit lower standard deviations (< 1.5 kg CH_4 yr^{-1} m^{-2}).

No clear increase of bubble seepage over the investigation time is evident (Fig. 2). Nor is there a trend of increasing seabed temperature. However, increased bottom water temperatures are associated with increased fluxes and vice versa at the Slope-Area, except for the period between S3 and S4. This correlation could be attributed to shallow hydrate formation/dissociation due to bottom water temperature fluctuations. However, our temperature data do not reveal the duration of heat pulses prior to acoustic measurement and thus, any interpretation about bottom water temperature influencing gas hydrate occurrence remains speculative. Large and rapid temperature changes have been reported for this area (Berndt et al., 2014); such changes are unlikely to penetrate the sediment sufficiently to drive hydrate formation/dissociation. In addition, hydrate is unlikely to be present very close to the seabed, so gas hydrate decomposition is unlikely to be an important factor in the observed temporal variation of bubble fluxes.

Instead, we hypothesize that the observed changes are controlled by two environmental driving forces: *a) Hydrostatic pressure changes.* Hydrostatic pressure influences the sediment effective stress, controlling bubble seepage through the activation of previously non-active pore throats (Boles et al., 2001) and/or the dilation of conduits and/or fractures (Scandella et al., 2011). Bubble seepage modulation by hydrostatic pressure changes has been shown to be driven in shallow waters by high-amplitude and long-period ocean waves related to tidal cycles (Römer et al., 2016), storms (Shakhova et al., 2014), and tsunamis (Lapham et al., 2013). Additionally, atmospheric pressure fluctuations have been shown to control bubble-seepage (Mattson & Likens, 1990). *b) Tectonic activity.* Pressure waves produced by earthquakes have the potential to increase the sediment pore pressure and therefore create, close, or reactivate gas/fluid migration pathways (Judd & Hovland, 2009; Plaza-Faverola et al., 2015). Resulting overpressure could initiate capillary gas migration or seepage of trapped gas due to mechanical failure (Fischer et al., 2013). Hence, earthquakes may cause a redistribution of the resistance/capacitance system associated with the gas/fluid pathway network fed by a common reservoir. This redistribution may directly affect the seepage spatial distribution and the intensity of the seepage (Leifer & Boles, 2005). Increased bubbling and dissolved CH_4 concentrations in the bottom water have been previously linked to tectonic events (Fischer et al., 2013; Obzhirov et al., 2004) and as the study area is close to the tectonically active Molloy-Knipovich ridge system (4-8 earthquakes per year; SI, Table SI6), we hypothesize that earthquakes influence the gas emissions. These two mechanisms are summarized in the conceptual model of Fig. 3 for the PKF area west of Svalbard. So far, this hypothesis remains speculative since our hydroacoustic dataset lacks continuous records (see correlation attempt in SI; Texts SI6 and SI7) and is thus unable to associate bubble seepage to the postulated trigger mechanisms. Long-term continuous records would be needed to validate this hypothesis.

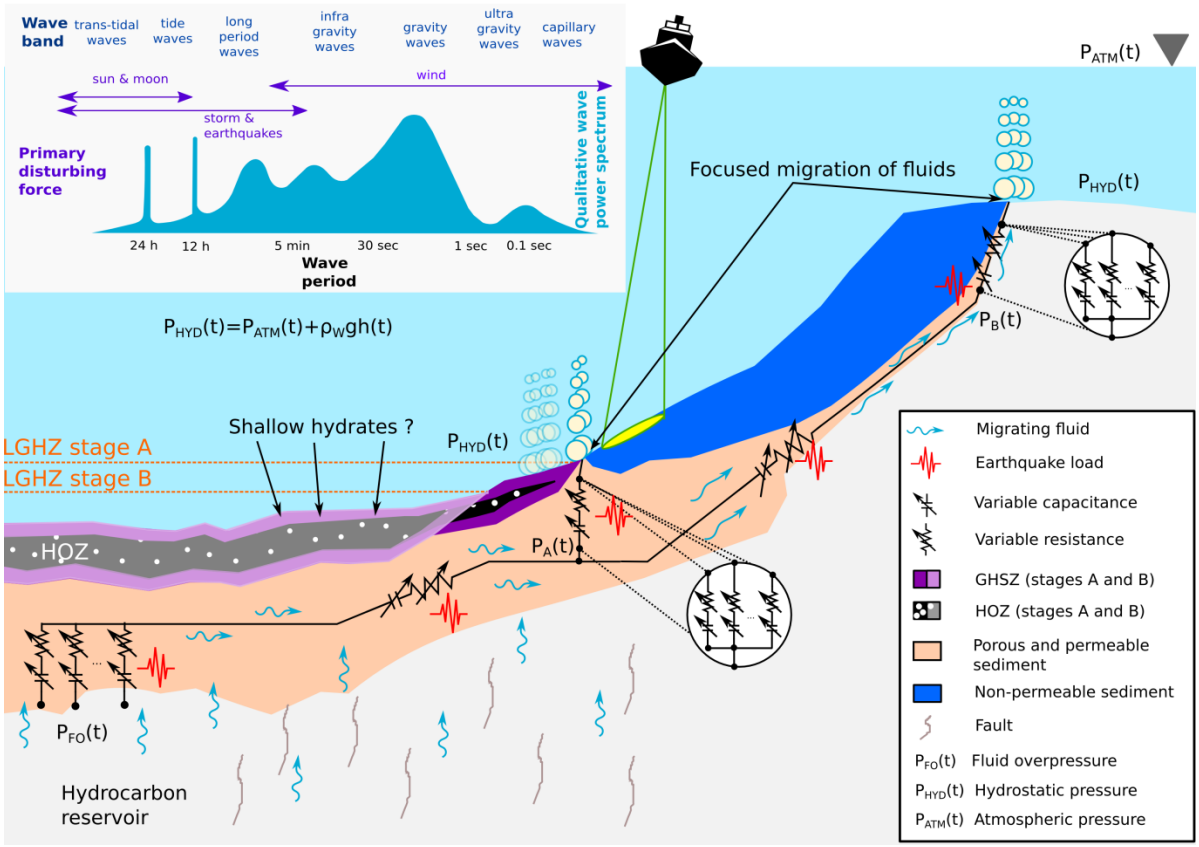

Figure 3. Conceptual model of natural driving mechanisms controlling bubble seepage offshore PKF. The schematic illustrates the hypothesized control mechanisms: a) hydrostatic pressure changes over bubble-vents; b) modification of gas migration pathway network triggered by earthquakes. The model is inspired by the high-resolution seismic studies of Rajan et al. (2012) and Sarkar et al. (2012) and an electrical model of a conduit network (Leifer & Boles, 2005). Additionally, a hypothetical spatial shift of bubble seepage triggered by an eventual long-term ocean warming scenario is shown. The figure illustrates the downward migration of the GHSZ and the hydrate occurrence zone (HOZ) from cooler (A) to warmer (B) bottom water temperature. The top left inset graph shows the ocean wave period spectra and the associated qualitative power spectrum to highlight wave periods with large effect on hydrostatic pressure.

3.3 Sub-seafloor fluid network

Increased fluxes in SBreak-Area correlate with decreased fluxes in Slope-Area, except for surveys S8 and S9 (Fig. 2). Thus, we suggest that the two areas are connected in the sub-seafloor and form parts of the same fluid migration system. Given the tectonic activity in the region, the observed alternating fluxes could be a result of changing resistance/capacitance of a joint fluid migration network (Fig. 3). Alternatively, hydrate formation/dissociation could cause blocking/opening of conduits feeding seepage areas further upslope. When pathways downslope are open, less gas will be supplied to the upslope seep area, resulting in alternating seepage intensity between SBreak-Area and Slope-Area.

3.4. Seepage migration at the LGHZ

A seasonal lateral shift of ca. 2 km of the LGHZ at Slope-Area (from 360 to 410 mbsl) was predicted between summer 2011 and winter 2012 as a response to bottom-water temperature fluctuations (Berndt et al., 2014). Seepage migration associated with this lateral shift, and in general to seasonal

modulation of the LGHZ, can be expected only if: a) shallow hydrates are present; b) a seasonal heat pulse reaches and destabilizes hydrates; c) new unimpeded gas pathways downslope exist or can form rapidly. Our surveys occurred during summer and autumn, and although bottom-water temperatures differed between the surveys, the seep site/flare spatial distribution near the LGHZ remained unaltered. This observation supports that seasonal hydrate formation/dissociation, if exist, did not influence the bubble-seepage spatial distribution. Unfortunately, the same observation does not prove or disprove seasonal shallow hydrate formation/dissociation, since even if this process is taking place, gas migrating towards the seabed could remain trapped in the sediment. An alternative hypothesis is that CH_4-seepage is mainly fed by sources in deeper sediment strata and its upward migration is mainly controlled by geological features. Based on the low probability of shallow hydrate presence, the time required for a heat pulse to migrate into the sediment, and our results showing unaltered distribution of bubble seepage, we suggest that seepage at this location is explained by the second hypothesis. We do not exclude that bubble-seepage offshore PKF could be partly influenced by hydrate dissociation triggered by ocean warming and therefore it may spatially migrate. However, hydrates are more likely to respond to longer time scale bottom water temperature changes (centennial to millennial) but also sea level changes could compensate their dissociation effects.

4 Conclusions

The analyses of 11 hydroacoustic seep surveys offshore PKF between 2008 and 2014 showed no significant trend in flux or spatial migration of seep locations. Mean yearly CH_4 free gas fluxes at the Shelf break (~240 mbsl.) are 3 kg CH_4 m^{-2} yr^{-1}, while 1.5 kg CH_4 m^{-2} yr^{-1} was obtained for the area close to the LGHZ in (~380 mbsl.). Mean fluxes and flow rates provide validated average values that consider short (days, weeks; duration of cruises) and long term (month and years) natural fluctuations; these may be considered for future modeling of methane input to the Arctic Ocean. The observed interconnectivity between seepage areas supports that seepage is controlled by focused migration pathways (Rajan et al., 2012; Sarkar et al., 2012). Our data analysis shows that ship-based hydroacoustic methods can be an efficient tool for repeated monitoring of bubble release. Applied in a standardized way it will help to establish the response of gas rich sediments to internal and external forcing mechanisms in the Arctic and elsewhere. Increasing water temperatures are likely to have a long-term impact on gas release intensity and the seep distribution offshore PKF; for a conclusive study this would require long-time observations most likely in an international effort with standardized methods.

Acknowledgments and Data

We are thankful for the support given by the crew -embers of RV Helmer Hanssen (UiT the Arctic University of Norway, N-9037 Tromsø) and RRS James Clark Ross (British Antarctic Survey). M. Veloso and J. Greinert both received support via COST Action ES0902 (PERGAMON) to join research cruises and acquire data. M. Veloso thanks the ERASMUS Mundus program of the EU (grant VECCEU) and the BECAS CHILE: CONICYT PAI/INDUSTRIA 79090016” program of the Chilean government. P. Jansson was supported by the Centre of Excellence: Arctic Gas Hydrate, Environment and Climate (CAGE) funded by the Norwegian Research Council (grant no. 223259). Data acquisition on RRS James Clark Ross was supported by Natural Environment Research Council grants NE/D005728, NE/H002732/1 and NE/H022260/1. We thank Joana Beja De Almeida E Silva for giving us technical support with data supplied by the National Oceanography Centre. EK60 data are available at (here PANGEA link). This is publication XXX of the Deep Sea Monitoring Group at GEOMAR.

References

Andreassen, K., Hubbard, A., Winsborrow, M., Patton, H., Vadakkepuliyambatta, S., Plaza-Faverola, A.,… Bünz, S. (2017). Massive blow-out craters formed by hydrate-controlled methane expulsion from the Arctic seafloor. *Science*, *356*(6341), 948–953. https://doi.org/10.1126/science.aal4500

Berndt, C., Feseker, T., Treude, T., Krastel, S., Liebetrau, V., Niemann, H., … Steinle, L. (2014). Temporal Constraints on Hydrate-Controlled Methane Seepage off Svalbard. *Science*, *343*(6168), 284–287. https://doi.org/10.1126/science.1246298

Biastoch, A., Treude, T., Rüpke, L. H., Riebesell, U., Roth, C., Burwicz, E. B., … Wallmann, K. (2011). Rising Arctic Ocean temperatures cause gas hydrate destabilization and ocean acidification. *Geophysical Research Letters*, *38*(8), L08602. https://doi.org/10.1029/2011GL047222

Boetius, A., & Wenzhöfer, F. (2013). Seafloor oxygen consumption fuelled by methane from cold seeps. *Nature Geoscience*, *6*(9), 725–734. https://doi.org/10.1038/ngeo1926

Boles, J. R., Clark, J. F., Leifer, I., & Washburn, L. (2001). Temporal variation in natural methane seep rate due to tides, Coal Oil Point area, California. *Journal of Geophysical Research: Oceans*, *106*(C11), 27077–27086. https://doi.org/10.1029/2000JC000774

Fischer, D., Mogollón, J. M., Strasser, M., Pape, T., Bohrmann, G., Fekete, N., … Kasten, S. (2013). Subduction zone earthquake as potential trigger of submarine hydrocarbon seepage. *Nature Geoscience*, *6*(8), 647–651. https://doi.org/10.1038/ngeo1886

Fisher, R. E., Sriskantharajah, S., Lowry, D., Lanoisellé, M., Fowler, C. M. R., James, R. H., … Nisbet, E. G. (2011). Arctic methane sources: Isotopic evidence for atmospheric inputs. *Geophysical Research Letters*, *38*(21), L21803. https://doi.org/10.1029/2011GL049319

Foote, K. G. (1987). Calibration of acoustic instruments for density estimation: a practical guide. *Int. Counc. Explor. Sea. Coop. Res. Rep.*, *144*, 57p.

Gentz, T., Damm, E., Schneider von Deimling, J., Mau, S., McGinnis, D. F., & Schlüter, M. (2014). A water column study of methane around gas flares located at the West Spitsbergen continental margin. *Continental Shelf Research*, *72*, 107–118. https://doi.org/10.1016/j.csr.2013.07.013

Graves, C. A., Steinle, L., Rehder, G., Niemann, H., Connelly, D. P., Lowry, D., … James, R. H. (2015). Fluxes and fate of dissolved methane released at the seafloor at the landward limit of the gas hydrate stability zone offshore western Svalbard. *Journal of Geophysical Research: Oceans*, *120*(9), 6185–6201. https://doi.org/10.1002/2015JC011084

Hornafius, J. S., Quigley, D., & Luyendyk, B. P. (1999). The world's most spectacular marine hydrocarbon seeps (Coal Oil Point, Santa Barbara Channel, California): Quantification of emissions. *Journal of Geophysical Research: Oceans*, *104*(C9), 20703–20711. https://doi.org/10.1029/1999JC900148

James, R. H., Bousquet, P., Bussmann, I., Haeckel, M., Kipfer, R., Leifer, I., … Greinert, J. (2016). Effects of climate change on methane emissions from seafloor sediments in the Arctic Ocean: A review. *Limnology and Oceanography*, n/a-n/a. https://doi.org/10.1002/lno.10307

Judd, A. G., & Hovland, M. (2009). *Seabed fluid flow: the impact of geology, biology and the marine environment* (Digitally print. version). New York, NY: Cambridge Univ. Press.

Kvenvolden, K. A. (1993). Gas hydrates—geological perspective and global change. *Reviews of Geophysics*, *31*(2), 173–187.

Lapham, L., Wilson, R., Riedel, M., Paull, C. K., & Holmes, M. E. (2013). Temporal variability of in situ methane concentrations in gas hydrate-bearing sediments near Bullseye Vent, Northern Cascadia Margin. *Geochemistry, Geophysics, Geosystems*, *14*(7), 2445–2459. https://doi.org/10.1002/ggge.20167

Leifer, I., & Boles, J. (2005). Measurement of marine hydrocarbon seep flow through fractured rock and unconsolidated sediment. *Marine and Petroleum Geology*, *22*(4), 551–568. https://doi.org/10.1016/j.marpetgeo.2004.10.026

Leifer, I., Patro, R. K., & Bowyer, P. (2000). A Study on the Temperature Variation of Rise Velocity for Large Clean Bubbles. *Journal of Atmospheric and Oceanic Technology*, *17*(10), 1392–1402. https://doi.org/10.1175/1520-0426(2000)017<1392:ASOTTV>2.0.CO;2

Leifer, I., Solomon, E., Schneider von Deimling, J., Rehder, G., Coffin, R., & Linke, P. (2015). The fate of bubbles in a large, intense bubble megaplume for stratified and unstratified water: Numerical simulations of 22/4b expedition field data. *Marine and Petroleum Geology*, *68*, 806–823. https://doi.org/10.1016/j.marpetgeo.2015.07.025

Leifer, I., & Patro, R. K. (2002). The bubble mechanism for methane transport from the shallow sea bed to the surface: A review and sensitivity study. *Continental Shelf Research*, *22*(16), 2409–2428. https://doi.org/10.1016/S0278-4343(02)00065-1

Lund Myhre, C., Ferré, B., Platt, S. M., Silyakova, A., Hermansen, O., Allen, G., … Mienert, J. (2016). Extensive release of methane from Arctic seabed west of Svalbard during summer 2014 does not influence the atmosphere. *Geophysical Research Letters*, 2016GL068999. https://doi.org/10.1002/2016GL068999

Mattson, M. D., & Likens, G. E. (1990). Air pressure and methane fluxes. *Nature*, *347*(6295), 718–719. https://doi.org/10.1038/347718b0

Mau, S., Römer, M., Torres, M. E., Bussmann, I., Pape, T., Damm, E., … Bohrmann, G. (2017). Widespread methane seepage along the continental margin off Svalbard - from Bjørnøya to Kongsfjorden. *Scientific Reports*, *7*, 42997. https://doi.org/10.1038/srep42997

Mendelson, H. D. (1967). The prediction of bubble terminal velocities from wave theory. *AIChE Journal*, *13*(2), 250–253. https://doi.org/10.1002/aic.690130213

Nilsen, F., Skogseth, R., Vaardal-Lunde, J., & Inall, M. (2016). A Simple Shelf Circulation Model: Intrusion of Atlantic Water on the West Spitsbergen Shelf. *Journal of Physical Oceanography*, *46*(4), 1209–1230. https://doi.org/10.1175/JPO-D-15-0058.1

Obzhirov, A., Shakirov, R., Salyuk, A., Suess, E., Biebow, N., & Salomatin, A. (2004). Relations between methane venting, geological structure and seismo-tectonics in the Okhotsk Sea. *Geo-Marine Letters*, *24*(3), 135–139. https://doi.org/10.1007/s00367-004-0175-0

O'Connor, F. M., Boucher, O., Gedney, N., Jones, C. D., Folberth, G. A., Coppell, R., … Johnson, C. E. (2010). Possible role of wetlands, permafrost, and methane hydrates in the methane cycle under future climate change: A review. *Reviews of Geophysics*, *48*(4), RG4005. https://doi.org/10.1029/2010RG000326

Pisso, I., Myhre, C. L., Platt, S. M., Eckhardt, S., Hermansen, O., Schmidbauer, N., … Stohl, A. (2016). Constraints on oceanic methane emissions west of Svalbard from atmospheric in situ measurements and Lagrangian transport modeling. *Journal of Geophysical Research. Atmospheres*, *121*(23), 14188–14200. https://doi.org/10.1002/2016JD025590

Plaza-Faverola, A., Bünz, S., Johnson, J. E., Chand, S., Knies, J., Mienert, J., & Franek, P. (2015). Role of tectonic stress in seepage evolution along the gas hydrate-charged Vestnesa Ridge, Fram Strait. *Geophysical Research Letters*, *42*(3), 2014GL062474. https://doi.org/10.1002/2014GL062474

Pohlman, J. W., Greinert, J., Ruppel, C., Silyakova, A., Vielstädte, L., Casso, M., … Bünz, S. (2017). Enhanced CO2 uptake at a shallow Arctic Ocean seep field overwhelms the positive warming potential of emitted methane. *Proceedings of the National Academy of Sciences*, *114*(21), 5355–5360. https://doi.org/10.1073/pnas.1618926114

Pohlman, J. W., Bauer, J. E., Waite, W. F., Osburn, C. L., & Chapman, N. R. (2011). Methane hydrate-bearing seeps as a source of aged dissolved organic carbon to the oceans. *Nature Geoscience*, *4*(1), 37–41. https://doi.org/10.1038/ngeo1016

Portnov, A., Vadakkepuliyambatta, S., Mienert, J., & Hubbard, A. (2016). Ice-sheet-driven methane storage and release in the Arctic. *Nature Communications*, *7*, 10314. https://doi.org/10.1038/ncomms10314

Rajan, A., Mienert, J., & Bünz, S. (2012). Acoustic evidence for a gas migration and release system in Arctic glaciated continental margins offshore NW-Svalbard. *Marine and Petroleum Geology*, *32*(1), 36–49. https://doi.org/10.1016/j.marpetgeo.2011.12.008

Römer, M., Sahling, H., Pape, T., Bahr, A., Feseker, T., Wintersteller, P., & Bohrmann, G. (2012). Geological control and magnitude of methane ebullition from a high-flux seep area in the Black Sea—the Kerch seep area. *Marine Geology*, *319–322*, 57–74. https://doi.org/10.1016/j.margeo.2012.07.005

Römer, M., Sahling, H., Pape, T., dos Santos Ferreira, C., Wenzhöfer, F., Boetius, A., & Bohrmann, G. (2014). Methane fluxes and carbonate deposits at a cold seep area of the Central Nile Deep Sea Fan, Eastern Mediterranean Sea. *Marine Geology*, *347*, 27–42. https://doi.org/10.1016/j.margeo.2013.10.011

Römer, M., Riedel, M., Scherwath, M., Heesemann, M., & Spence, G. D. (2016). Tidally controlled gas bubble emissions: A comprehensive study using long-term monitoring data from the NEPTUNE cabled observatory offshore Vancouver Island. *Geochemistry, Geophysics, Geosystems*, *17*(9), 3797–3814. https://doi.org/10.1002/2016GC006528

Römer, M., Sahling, H., Pape, T., Bohrmann, G., & Spieß, V. (2012). Quantification of gas bubble emissions from submarine hydrocarbon seeps at the Makran continental margin (offshore Pakistan). *Journal of Geophysical Research: Oceans*, *117*(C10), C10015. https://doi.org/10.1029/2011JC007424

Ruppel, C. D., & Kessler, J. D. (2017). The interaction of climate change and methane hydrates. *Reviews of Geophysics*, *55*(1), 2016RG000534. https://doi.org/10.1002/2016RG000534

Sahling, H., Römer, M., Pape, T., Bergès, B., dos Santos Fereirra, C., Boelmann, J., … Bohrmann, G. (2014). Gas emissions at the continental margin west of Svalbard: mapping, sampling, and quantification. *Biogeosciences*, *11*(21), 6029–6046. https://doi.org/10.5194/bg-11-6029-2014

Sarkar, S., Berndt, C., Minshull, T. A., Westbrook, G. K., Klaeschen, D., Masson, D. G., … Thatcher, K. E. (2012). Seismic evidence for shallow gas-escape features associated with a retreating gas hydrate zone offshore west Svalbard. *Journal of Geophysical Research: Solid Earth*, *117*(B9), B09102. https://doi.org/10.1029/2011JB009126

Sauter, E. J., Muyakshin, S. I., Charlou, J.-L., Schlüter, M., Boetius, A., Jerosch, K., … Klages, M. (2006). Methane discharge from a deep-sea submarine mud volcano into the upper water column by gas hydrate-coated methane bubbles. *Earth and Planetary Science Letters*, *243*(3–4), 354–365. https://doi.org/10.1016/j.epsl.2006.01.041

Scandella, B. P., Varadharajan, C., Hemond, H. F., Ruppel, C., & Juanes, R. (2011). A conduit dilation model of methane venting from lake sediments. *Geophysical Research Letters*, *38*(6), L06408. https://doi.org/10.1029/2011GL046768

Schneider von Deimling, J., Rehder, G., Greinert, J., McGinnnis, D. F., Boetius, A., & Linke, P. (2011). Quantification of seep-related methane gas emissions at Tommeliten, North Sea. *Continental Shelf Research*, *31*(7–8), 867–878. https://doi.org/10.1016/j.csr.2011.02.012

Shakhova, N., Semiletov, I., Salyuk, A., Yusupov, V., Kosmach, D., & Gustafsson, Ö. (2010). Extensive Methane Venting to the Atmosphere from Sediments of the East Siberian Arctic Shelf. *Science*, *327*(5970), 1246–1250. https://doi.org/10.1126/science.1182221

Shakhova, N., Semiletov, I., Leifer, I., Sergienko, V., Salyuk, A., Kosmach, D., … Gustafsson, Ö. (2014). Ebullition and storm-induced methane release from the East Siberian Arctic Shelf. *Nature Geoscience*, *7*(1), 64–70. https://doi.org/10.1038/ngeo2007

Steinle, L., Graves, C. A., Treude, T., Ferré, B., Biastoch, A., Bussmann, I., … Niemann, H. (2015). Water column methanotrophy controlled by a rapid oceanographic switch. *Nature Geoscience*, *8*(5), 378–382. https://doi.org/10.1038/ngeo2420

Steinle, L., Schmidt, M., Bryant, L., Haeckel, M., Linke, P., Sommer, S., … Niemannn, H. (2016). Linked sediment and water-column methanotrophy at a man-made gas blowout in the North Sea:

Implications for methane budgeting in seasonally stratified shallow seas. *Limnology and Oceanography*, *61*(S1), S367–S386. https://doi.org/10.1002/lno.10388

Torres, M. E., McManus, J., Hammond, D. E., de Angelis, M. A., Heeschen, K. U., Colbert, S. L., … Suess, E. (2002). Fluid and chemical fluxes in and out of sediments hosting methane hydrate deposits on Hydrate Ridge, OR, I: Hydrological provinces. *Earth and Planetary Science Letters*, *201*(3–4), 525–540. https://doi.org/10.1016/S0012-821X(02)00733-1

Veloso, M., Greinert, J., Mienert, J., & De Batist, M. (2015). A new methodology for quantifying bubble flow rates in deep water using splitbeam echosounders: Examples from the Arctic offshore NW-Svalbard: Quantifying bubble flow rates in deep water. *Limnology and Oceanography: Methods*, *13*(6), 267–287. https://doi.org/10.1002/lom3.10024

Westbrook, G. K., Thatcher, K. E., Rohling, E. J., Piotrowski, A. M., Pälike, H., Osborne, A. H., … Aquilina, A. (2009). Escape of methane gas from the seabed along the West Spitsbergen continental margin. *Geophysical Research Letters*, *36*(15), L15608. https://doi.org/10.1029/2009GL039191

Woolf, D. K. (1993). Bubbles and the air-sea transfer velocity of gases. *Atmosphere-Ocean*, *31*(4), 517–540. https://doi.org/10.1080/07055900.1993.9649484

Woolf, D. K., & Thorpe, S. A. (1991). Bubbles and the air-sea exchange of gases in near-saturation conditions. *Journal of Marine Research*, *49*(3), 435–466. https://doi.org/10.1357/002224091784995765

Yamamoto, A., Yamanaka, Y., Oka, A., & Abe-Ouchi, A. (2014). Ocean oxygen depletion due to decomposition of submarine methane hydrate. *Geophysical Research Letters*, *41*(14), 2014GL060483. https://doi.org/10.1002/2014GL060483

Geophysical Research Letters

Supporting Information for

Variability of seafloor methane emissions evidenced by repeated hydroacoustic surveys offshore Svalbard

M. E. Veloso-Alarcón[1,2]*, P. Jansson[3], M. De Batist[2], T. A. Minshull[4], G. Westbrook[5], H. Pälike[4], S. Bünz[3], I. Wright[6], J. Greinert[1,2,3]

[1]GEOMAR Helmholtz Centre for Ocean Research Kiel, Wischhofstr. 1-3 24148 Kiel, Germany.

[2]Renard Centre of Marine Geology, Ghent University, Krijgslaan 281 s.8 B-9000 Ghent, Belgium.
[3]CAGE-Centre for Arctic Gas Hydrate, Environment and Climate, Department of Geosciences, UiT- The Arctic University of Norway, Postboks 6050 Langnes, N-9037 Tromsø, Norway.
[4]National Oceanography Centre Southampton, University of Southampton, European Way, Southampton SO14 3ZH, United Kingdom.
[5]School of Geography, Earth and Environmental Sciences, University of Birmingham, Edgbaston, United Kingdom.
[6]Vice-Chancellor's Office, University of Canterbury, Private Bag 4800, Christchurch, New Zealand

Contents of this file

Additional Supporting Information (Files uploaded separately)

Excel file with CTD dataset

Matlab files and script to generate CTD profiles

Introduction

This supplementary material contains information about the echosounder data acquisition (Table SI1), its online availability and information about data processing methodology. The first data processing steps, leading to flow rate estimations are described in full detail in Veloso et al. (2015).

Text SI1.

Footprint of acoustic flares

Acoustic flares in SBES echograms appear when the echosounder beam insonifies single or multiple bubble streams. The acoustic backscattering increases as the echosounder beam approaches the bubbles, and reaches a maximum amplitude when the beam insonifies the maximum number of bubbles. Subsequently, the backscattering starts to decrease as the SBES beam moves away from the bubbles. The central pings of a flare (strongest backscattering; Fig. SI3) thus contain information about the maximum number of bubbles captured by the echosounder beam.

In order to calculate the flow rate of individual flares, we manually select backscatter values of the central pings within a layer 5-10 meters above the seafloor (selected matrix Fig. SI3). The representative target strength $\overline{TS}$ of the flare is calculated by the geometrical average of the acoustical cross-sections (which is the arithmetic mean of the target strength $TS_{i,j}$ of the samples included in the selection).

The $\overline{TS}$ represents the backscattering of a sample volume with dimensions of a truncated conical section vertically bounded by the sample thickness (derived from the sampling interval and the sound speed in the water). Thus, we interpret that the calculated flare flow rate derived from$\overline{TS}$corresponds to bubbles within a virtual sample volume (Fig. SI3) for which the dimensions and central position are derived from the average information of the samples within the selection. The geo-referenced central position of the virtual sample given by$\overline{X}$, $\overline{Y}$ and $\overline{Z}$ is obtained from the arithmetic mean of the sample in UTM coordinates and the water depth. Similarly, a radius$R_F$and a geo-referenced area $A_F$of the virtual flare footprint (which is assumed to be circular) were calculated using the average depth $\overline{Z}$ of the selected layer and the equivalent echosounder beam angle α_B (equations SI1.a and SI1.b).

$$R_F = \overline{Z} tan\left(\frac{\alpha_B}{2}\right) \quad \text{(SI1.a)}$$

$$A_F = \pi {R_F}^2 \quad \text{(SI1.b)}$$

The $\overline{TS}$ values used in our flare-flow rate calculations are restricted to an area not larger than$A_F$where the highest population of bubbles forming a flare can be found. Since clusters of bubble streams that originate flares may cover a surface larger than the echosounder footprint, the use of averaged target strengths is recognized to be a potential source of flow rate underestimations. Additionally, underestimation of flow rates can also occurs when the backscattering coming from a bubble stream cluster (or single bubble vent), with an areal coverage smaller than the footprint, is captured by a sector from the directivity pattern less sensitive than its axis.

Text SI2.

Bubble size distribution

Visual observation of bubbles at the study area were conducted during surveys S2 and S3 using a submersible video-camera system developed at NIOZ. Images were analyzed and used for bubble size measurements (McGovern 2012). As a result, a bubble size distribution (a required input in our inverse hydroacoustic method) was obtained from a total of 641 individual bubble observations (Fig. SI4).

Text SI3.

Bubble rising speed models

Bubble rising speed (Fig. SI5) were calculated using the bubble size spectra obtained from the visual information and a MATLAB script provided by Ira Leifer (Bubbleology Research International) which includes several bubble rise models (Mendelson 1967; Woolf and Thorpe 1991; Woolf 1993; Leifer et al. 2000; Leifer and Patro 2002, Leifer et al.,2015). Models consider both 'clean' and 'dirty' bubbles.

Text SI4.

Clustering of spatially overlapping flares

In order to assign an average flow rate to a cluster of flares forming a seep site, flares were clustered if their geo-referenced virtual footprints spatially overlapped at the average depth of the selected layer (Fig. SI6; Veloso et al., 2015). Once a cluster was found, the flux of each flare Q_{Fi} (flow rate normalized by the virtual footprint area; see Text SI1) was used to find an average cluster flux Q_C (equation SI2),

$$Q_C = \frac{1}{n_F}\sum_i^{n_F} Q_{Fi}, \quad \text{(SI2)}$$

where$n_F$represents the number of flares that form the cluster.

Finally, a flow rate of the cluster $F_C$can be calculated by multiplying the average cluster flux with the area covered by the cluster A_C (equation SI3)

$$F_C = Q_C A_C \quad \text{(SI3)}$$

Text SI5.

Common Area Flux Method (CAF Method)

The temporal analysis of seep activity is based on the comparison of areas containing hydroacoustic data related to bubble release that have been repeatedly insonified during surveys (Figs. SI7 and SI8).

For this comparison, acoustic flares that belong to a survey with geographically overlapping beam-footprints were clustered and an average flux was assigned to each cluster (Text SI4). An average flux was obtained by normalizing the mean flow rate of all flares within the cluster with the cluster area. The georeferenced areas of all clusters were gridded in MATLAB using a cell size of 1x1 m and a mean flux of the cluster was assigned to each individual cluster cell. The common area including the flux per cell was extracted from the combination of the survey matrices (Fig. SI9) using commands of the Generic Mapping Tools (GMT; Wessel et al., 2013). A representative flux (Q_{RF}) was calculated using the arithmetic mean of the fluxes associated with the common area grids (equation 1).

$$Q_{RF} = \frac{\sum_j^m \sum_i^n q_{i,j}}{Ne} \quad [1]$$

Where,

$q_{i,j}$: Flux at the i, j grid

Ne : Number of cells with flux values

No grid cell was covered by all 11 surveys but small areas were covered by up to 8 surveys. For our analyses we included a total of 29 and 35 different combinations (min. two overlapping survey) for areas A1 and A2, respectively (Tables SI3 and SI4). The final mean flux (Q_{RF}) per survey was calculated by averaging the obtained representative flux values Q_{RF} within a survey.

Text SI6.

Correlation between results and changes of static pressure (tides, storms, tsunamis)

We hypothesize that hydrostatic pressure is a driving force affecting the gas seepage in the study area and therefore might be in part responsible for the gas emission fluctuations observed. To test this hypothesis we correlated TS values from area A1 (most densely surveyed area) with modeled sea surface tide-related heights (*SSH*) using the software TPXO (Egbert and Erofeeva 2002). Only flares observed several times were included in the tide correlation analysis. This filtering targets the temporal variability by excluding flares that are only observed once.

We normalize the target strength (*TS*) values with the footprint area and bin depth in order to find a non-biased backscatter value for the analysis. The resulting volume backscatter strength S_V is:

$$S_V = 10log_{10}\left(\frac{10^{\left(\frac{TS}{10}\right)}}{A_F ct/2}\right), \quad \text{(SI4)}$$

where A_F is the footprint area (m^2), c is the sound velocity (m/s) and t is the pulse length (s) of the echosounder transducer.

The standard deviation of S_V is high, yielding a low S_V/*SSH* correlation (r=0.0095, Fig. SI10). We also correlated the time-derivative of the modeled sea-surface-height (*dSSH/dt*, Fig.SI10) with S_V, in order to attribute pressure drop to observed free gas in the water column. Considering that it takes time for bubbles originating at some sediment depth to reach the water column where they are detected, we applied time lags to the S_V observations. These time-shifted S_V values and *dSSH/dt* correlate weakly, and for the best-fitted time lag of 75 minutes, the correlation is r=-0.1181 (Fig. SI10), giving little support to the hypothesis. We conclude that the presented data neither supports nor falsifies the hypothesis that gas emissions increase when hydrostatic pressure drops.

Text SI7.

Correlation between results and tectonic activity

Due to the proximity to the tectonically active Molloy-Knipovich ridge system (4-8 earthquakes per year; Table SI6), it is hypothesized that earthquakes may influence the CH4-bubble seepage at our study area. As fluid migration is thought to occur along near-horizontal permeable pathways connected to deeper reservoirs (Rajan et al., 2012; Sarkar et al., 2012), earthquake loading may influence the conduit network at deeper sedimentary sections closer to the spreading-ridge system. To test our hypothesis and arrive at a first order correlation between free gas flow and earthquake events, we used earthquake data (International Seismological Centre 2014) from the area 65°N – 90°N and 30°W - 30°E between Jan 1st 2008 and Dec 31st 2014. 8,589 corresponding earthquakes were found in the database and 7,443 had magnitudes given.

The local influence of remote or nearby earthquakes events with magnitude M and distance R from our study site is not well constrained because the earth structure is too complicated for such a quantity to be well defined. However, seismologists have done substantial work in order to derive ground motion prediction equations. In order to acquire a first order estimate of the local impact, we chose the simple equation of L. Esteva and E. Rosenblueth (1964) which is given in Douglas (2011) in order to have a first order estimate of the local acceleration.

$$a = ce^{\alpha M} R^{-\beta} \qquad \text{(SI5)}$$

Where a is the local acceleration (cm s^{-2}), c=2000, α=0.8 and β=2. M is the magnitude of the earthquake and R is the distance (km) from the epicenter or hypocenter. The magnitude M is taken from the downloaded dataset (isc.ac.uk), and the distance is calculated as the distance from the center of our study site to the earthquake position. The earthquake magnitudes are max=6.4, mean=2.0 with a standard deviation of 0.85. Fig. SI11 shows the calculated acceleration a (max=35.9, mean=0.3, std=1.1 cm s^{-2}) and observed TS (max=-23.7, min=-55 dB) from all nine included surveys. We did not observe any features in this data suggesting either positive or negative influence on the free gas observations. Dividing the dataset into nine “cruise subsets”, yields close-up analysis of the TS values vs. calculated local acceleration. No correlation between higher seismic activity and increased gas release or vice versa could be inferred from this analysis.

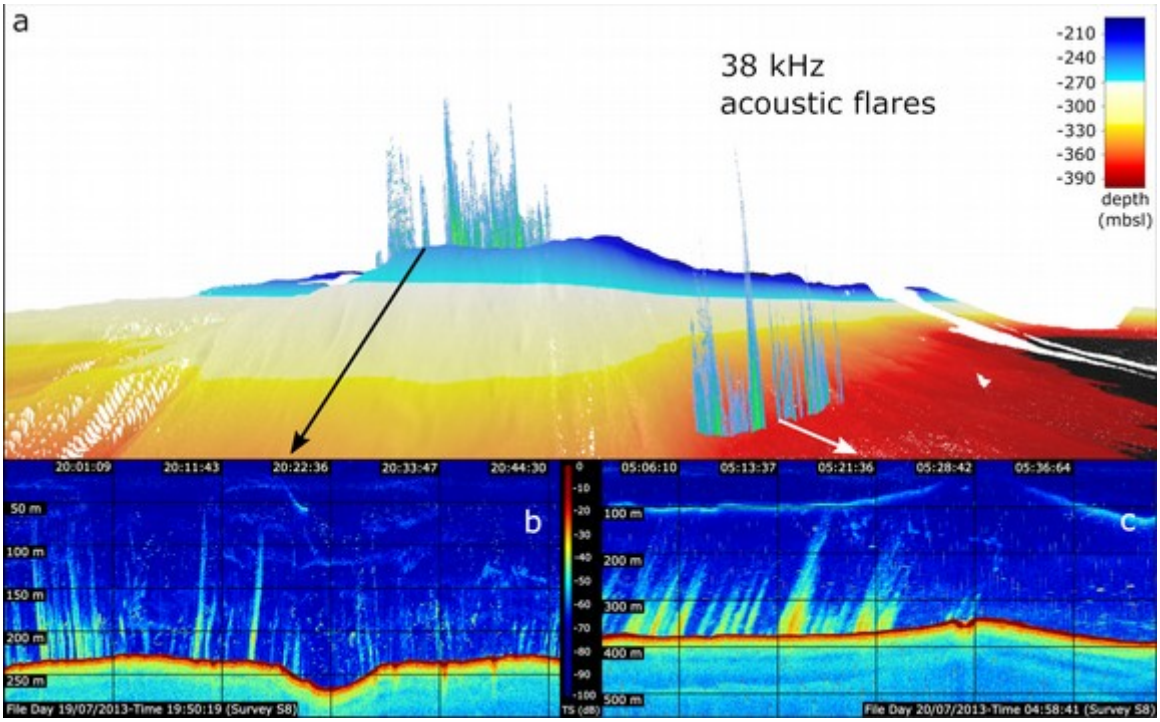

Figure SI1. Acoustic flares at PKF displayed in Fledermaus and Flarehunter GUI. a) 3-dimensional image produced with Fledermaus, showing flares and bathymetry. b, c) Echograms shown in Flarehunter GUI. Color scale indicates the Target strength (TS) of the backscatter signal. Flares are located at ~230 mbsl (SBreak-Area) and ~380 mbsl (Slope-Area).

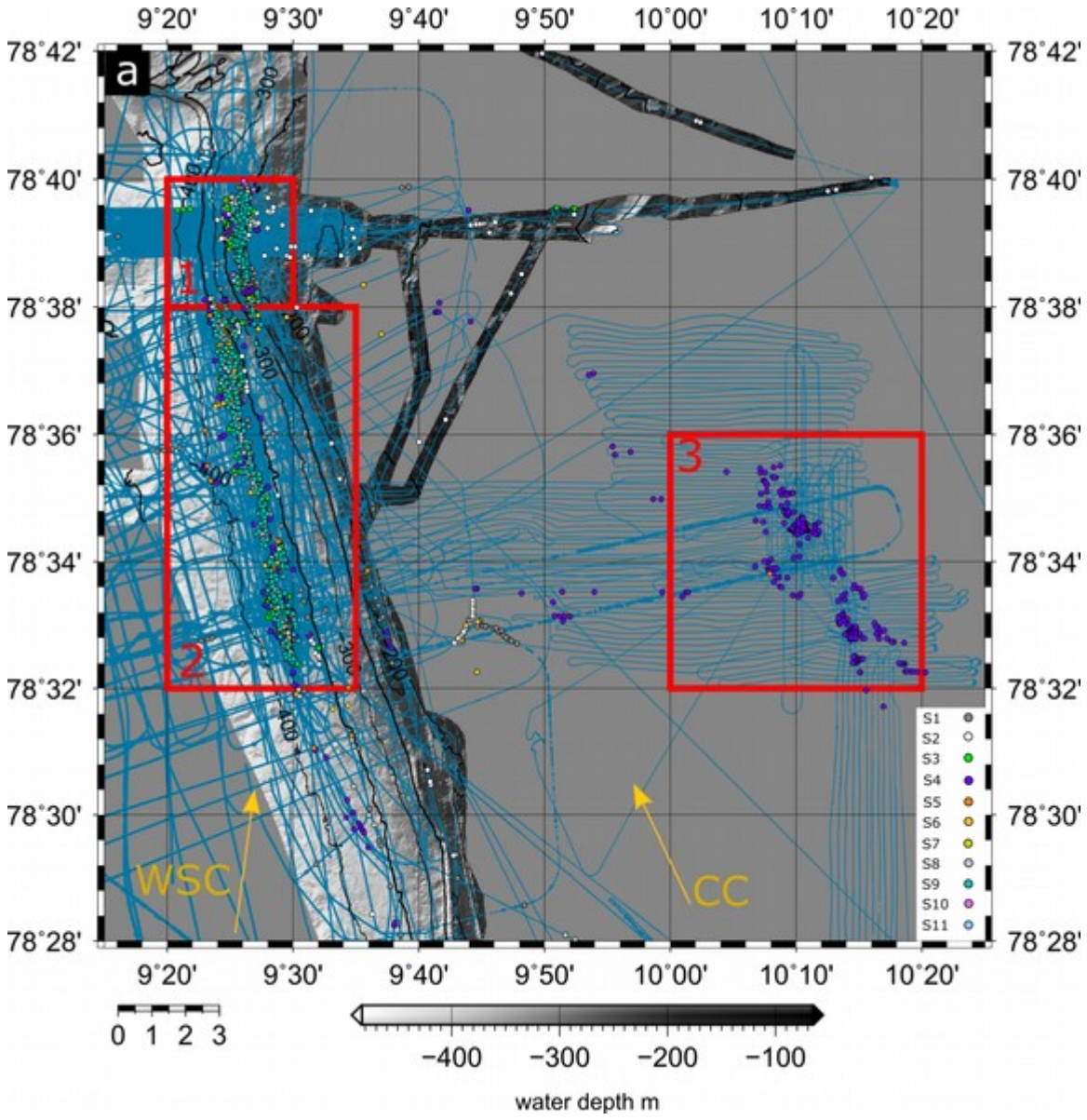

Figure SI2. Map of the study area. Gray scale shows the bathymetry and blue indicates the echosounder coverage at the seafloor. Colored dots indicate detected acoustic flares from different surveys. The red rectangles indicate the three defined sub-areas: (1) SBreak-Area, (2) Slope-Area, and (3) Shelf-Area). Yellow arrows indicate the influence of the West Spitsbergen Current (WSC) and the Coastal Current (CC).

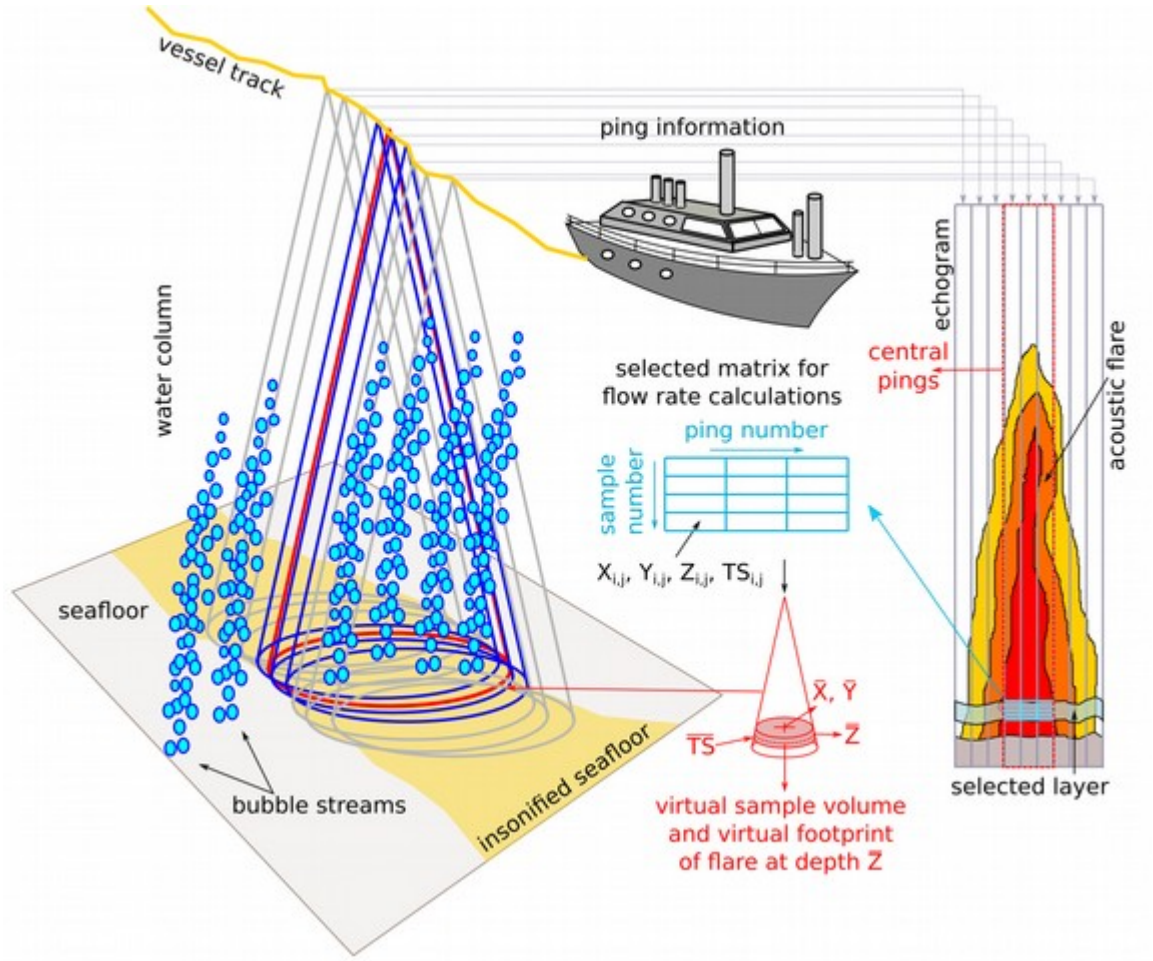

Figure SI3. Schematic illustrating the echosounder data collection, physical representation of a flare, data selection and the virtual footprint used in the flow rate calculations.

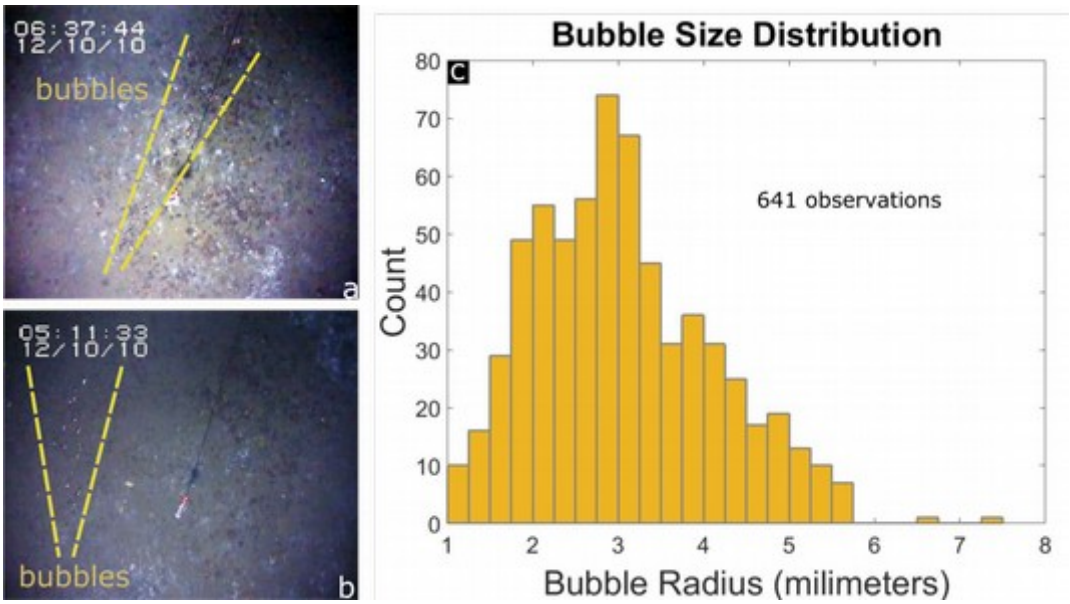

Figure SI4. a-b) examples of bubbles captured by the submersible video-camera system during survey S2. c) Bubble size distribution obtained from 641 bubble observations (Mc Govern, 2012)

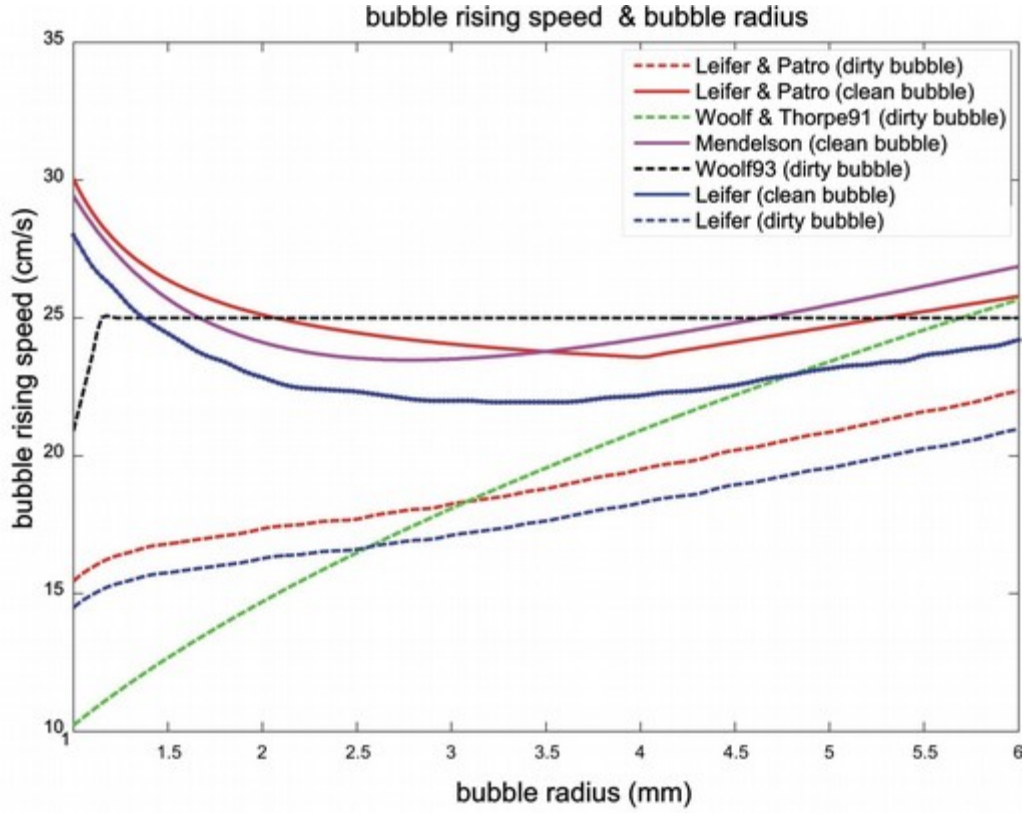

Figure SI5. Bubble rising speeds as functions of bubble radius (1 to 6 mm) using different models (Mendelson 1967; Woolf and Thorpe 1991; Woolf 1993; Leifer et al. 2000; Leifer and Patro 2002; Leifer et al., 2015). Figure from (Veloso et al. 2015).

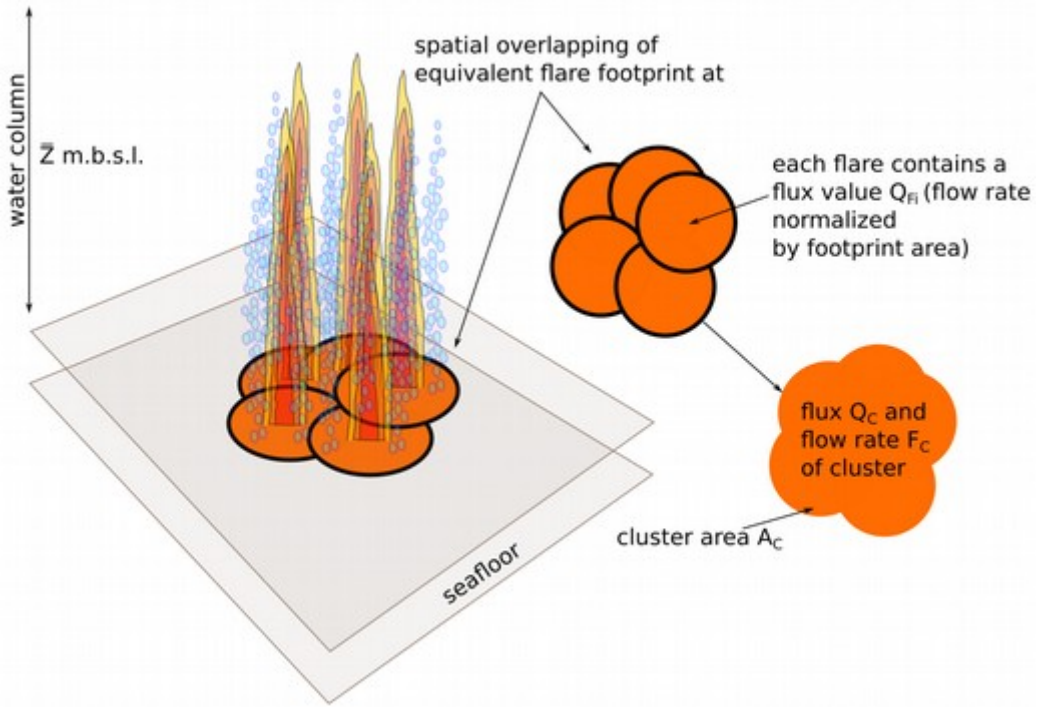

Figure SI6. Schematic illustrating the clustering process of acoustic flares that spatially overlap.

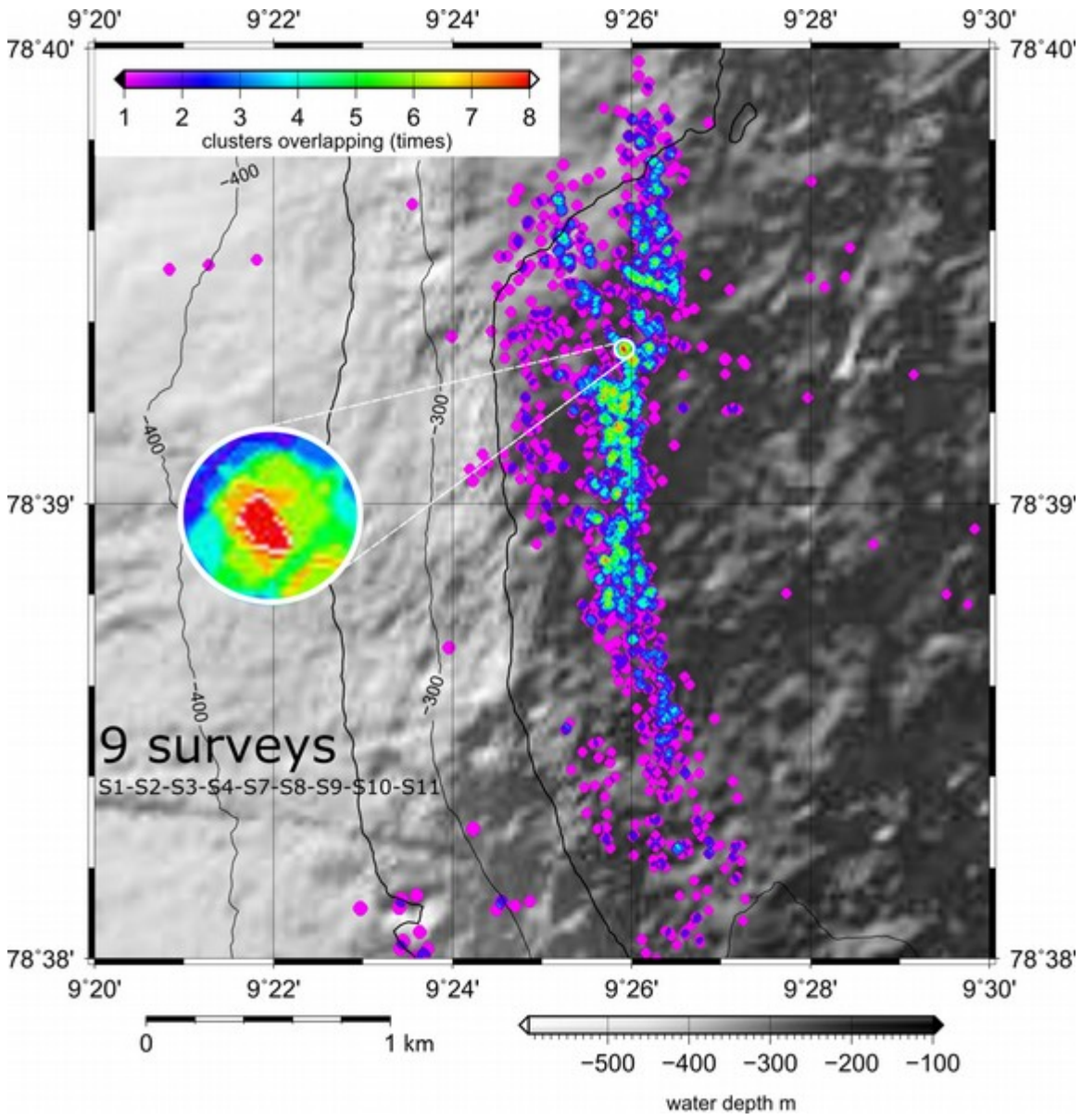

Figure SI7. Map of flare clusters in area A1. Colors indicate how many surveys that have identified the flare clusters. From 9 surveys (S1, S2, S3, S4, S7, S8, S9, S10, S11) the maximum overlap was 8 times.

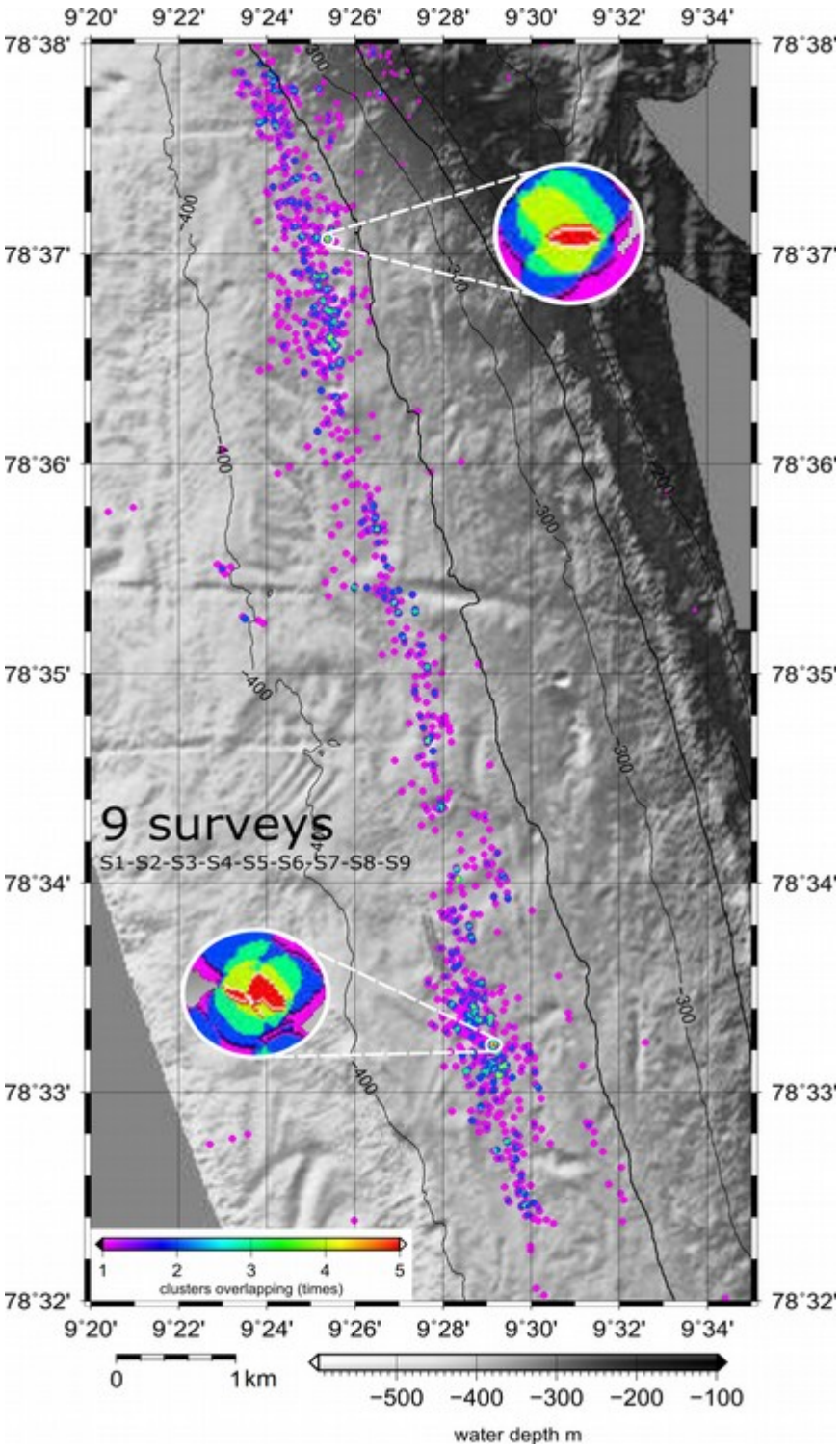

Figure SI8. Map of flare clusters in area A2. Colors indicate how many times flare clusters were covered during different surveys. From 9 surveys (S1, S2, S3, S4, S5, S6, S7, S8, S9) the maximum overlap obtained was 5 times.

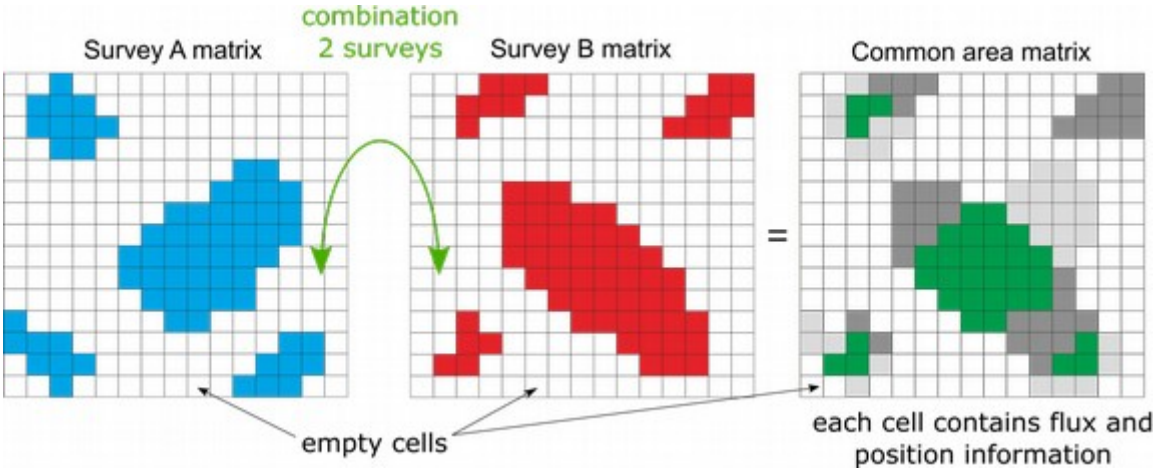

Figure SI9. Example of the combination of hydroacoustic information associated to bubble- seeping areas between two surveys.

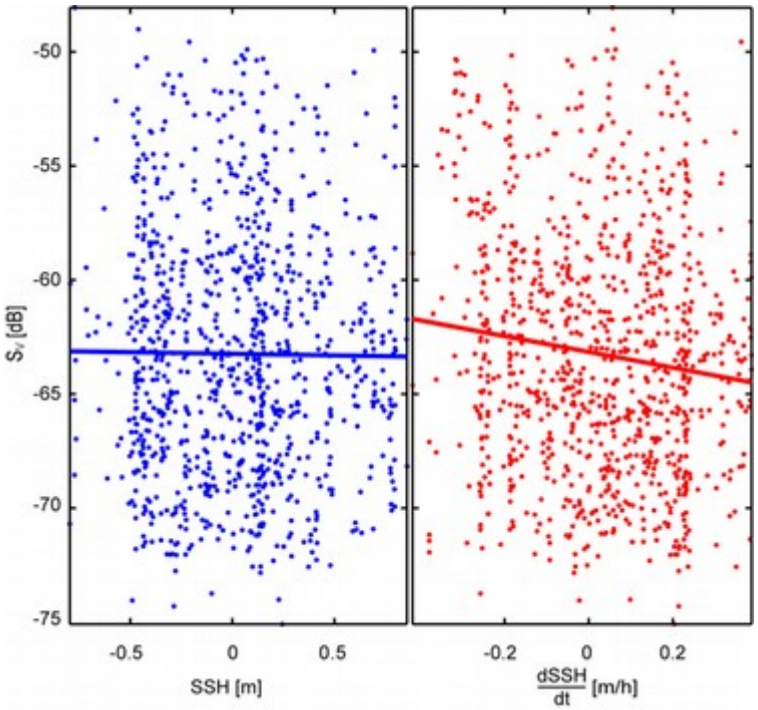

Figure SI10. Correlation between SSH and S_V. Left panel shows S_V values plotted against sea surface height (m) in blue dots and a linear regression as a blue line. Right panel shows S_V against the time derivative of SSH and a linear regression line (red dots and line).

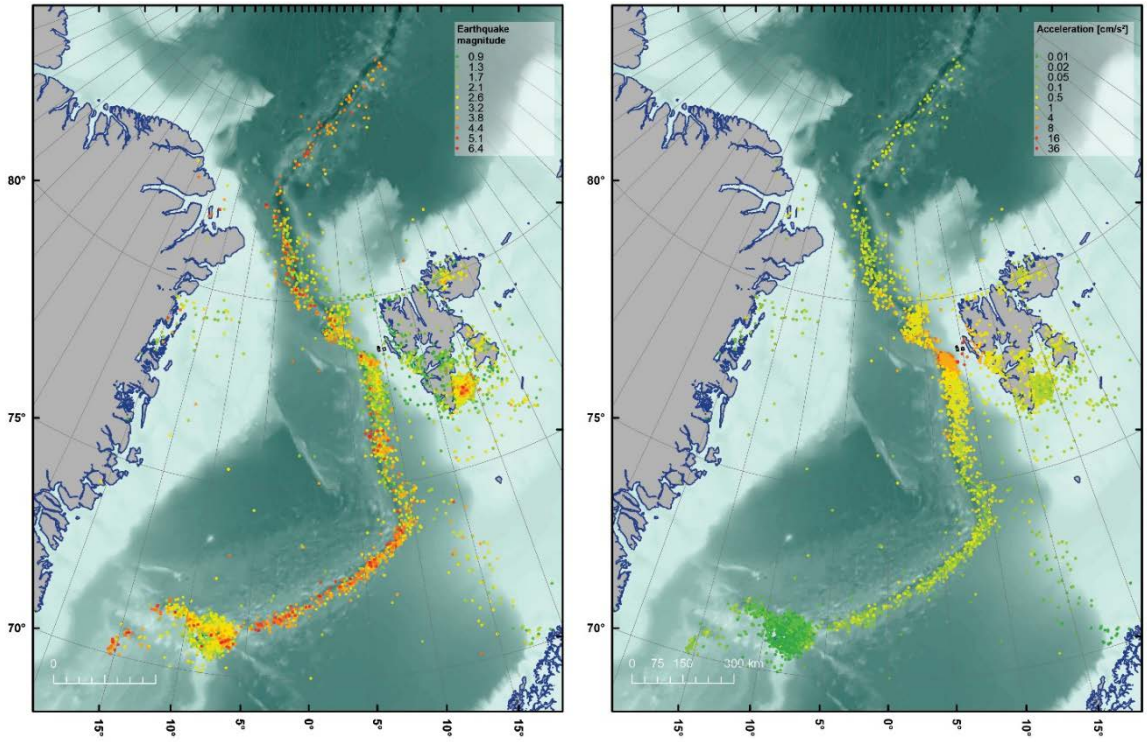

Figure SI11. Map of earthquake events. Left panel shows the earthquake Richter scale magnitude (mb, MC, MD or ML) and the right panel shows the local acceleration as calculated from equation 1 relative to the center of the study area.

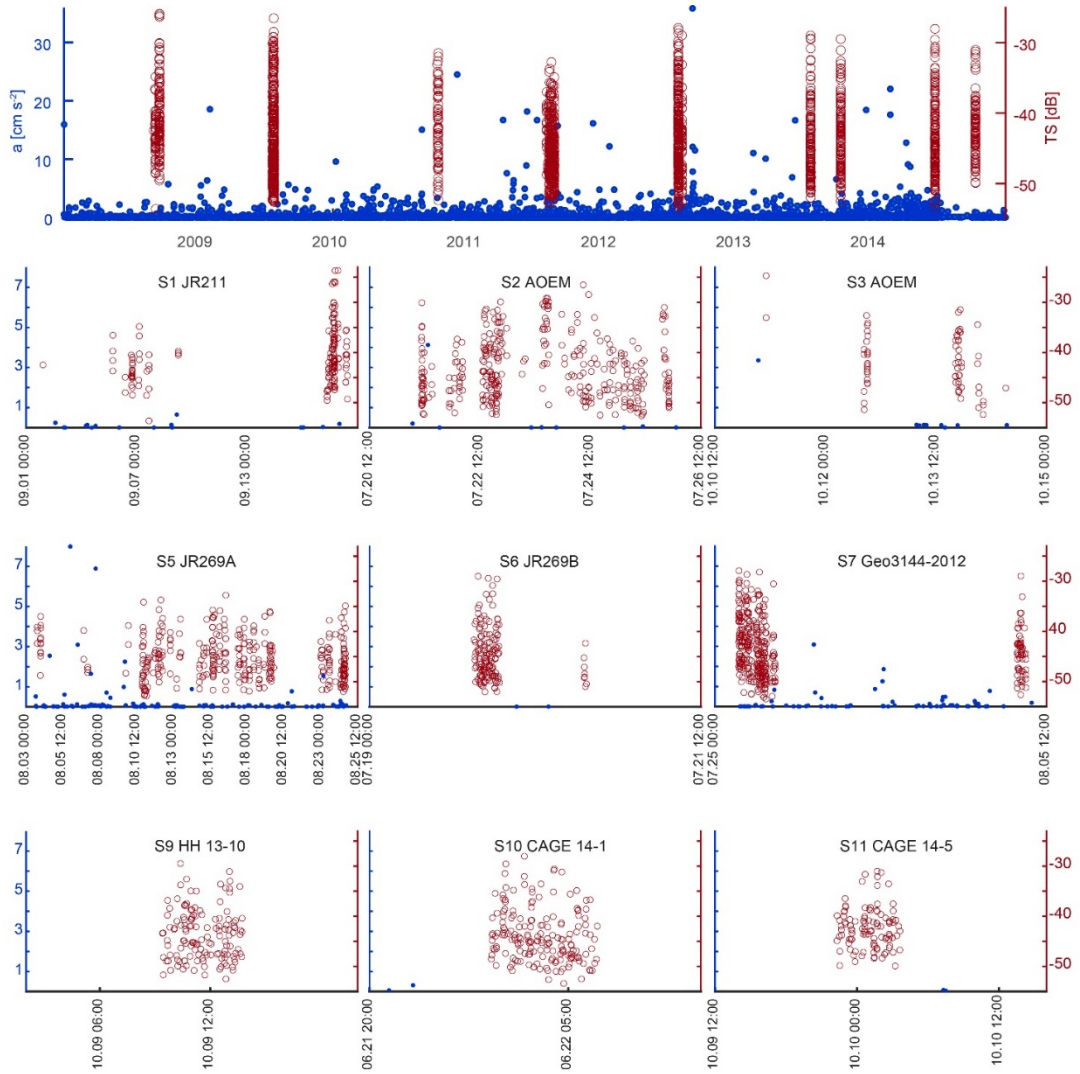

Figure SI12. Earthquake correlation with echosounder data. Blue dots are calculated accelerations (cm s^{-2}) (equation SI5) and the red circles denote TS values (dB) from the nine surveys in area A1.

Table SI1. List of hydroacoustic surveys considered in this study.

Survey number	Survey name	Month-year	Vessel
S1	JR211	August-2008	RV James Clark Ross
S2*	AOEM	July-2009	RV Helmer Hanssen
S3*	AOEM	October-2010	RV Helmer Hanssen
S4	JR253	July-2011	RV James Clark Ross
S5	JR269A	August-2011	RV James Clark Ross
S6	JR269B	July-2012	RV James Clark Ross
S7	Geo3144_2012	July-2012	RV Helmer Hanssen
S8	HH_13-7	July-2013	RV Helmer Hanssen
S9	HH_13-10	October-2013	RV Helmer Hanssen
S10	CAGE_14-1	June-2014	RV Helmer Hanssen
S11	CAGE 14_5	October-2014	RV Helmer Hanssen

*Surveys that include visual observations for BSD measurements (McGovern, 2012)

Table SI2. Water, gas and ambient constants used to evaluate flow rates of acoustic flares using the inverse hydroacoustic method

Constant Average	**Unit**	**Value**
Temperature water	C°	From CTD profiles (Excel File SI)
Static pressure at surface	Pa	101325
Water salinity	PSU	From CTD profiles (Excel File SI)
Water density	kg/m^3	From CTD profiles (Excel File SI)
Average sound speed in the water	m/s	From CTD profiles (Excel File SI . Del Grosso eq.)
Water shear viscosity	Pa·s	0.0014
Water surface tension	N/m	0.074
Gas density at the surface (CH_4)	kg/m^3	0.66
Acceleration of gravity	m/s^2	9.8
Specific heat capacity, CH_4	$J/(kg \cdot m^3)$	2191
Ratio of specific heat of gas	dimensionless	1.4

Table SI3. Common area fluxes for SBreak-Area. Fluxes are detailed for different surveys involved in the common area combination. All 29 combinations are shown. Average fluxes, standard deviation and relative errors are also detailed.

	S1	S2	S3	S4	S7	S8	S9	S10	S11	Common area (m^2)
Flux Kg/(yr·m^2)		7.16	1.67		2.96		7.61	2.89		5284
		9.39	3.80					6.19	2.41	9156
	1.15	8.02	3.33	4.06				6.80	4.05	8
		7.11			3.23					140924
		7.30			3.47	2.84	7.20			19512
					5.31	6.04	8.45	4.99	2.91	4916
		7.50				2.54	7.05			28708
		7.88						3.76		82248
		4.06						3.59	1.64	59612
		7.42		1.97	2.85					6708
					3.21	2.22	6.82			31588
						1.92	6.59			48960
								3.59	1.64	59612
	1.83	8.78	3.11				6.84	3.15		2868
	1.65	8.26	3.20		3.08	3.81				68
	1.34	10.09	3.57		5.48	3.59		6.34		1740
	2.34	8.97	3.81		4.62	3.41	6.10		6.10	1684
	1.40	8.45	3.35		3.97		7.36	3.37		2640
	1.22		3.72		5.35		7.74		1.83	1328
	2.88	7.98	3.67		3.62			4.52		5412
	2.85	8.25	3.91					4.94	1.93	2956
	1.76	7.16			2.96		7.61	2.89		5284
	2.32	7.47						3.48	1.91	9096
	1.28		3.12		3.78		7.25	3.49		3152
	2.19							3.24	1.66	15260
				1.49	2.61					15816
				2.35	2.76	3.22				3564
				2.07		2.16				7056
				2.05			7.68			5912
Mean	1.86	7.84	3.35	2.33	3.70	3.17	7.25	4.20	2.60	
Stdev	0.60	1.25	0.60	0.88	0.97	1.19	0.59	1.28	1.44	
Relative error (%)	26.99	10.75	11.67	24.90	21.22	24.92	6.30	25.48	40.21	

Table SI4. Common area fluxes for Slope-Area. Fluxes are detailed for different surveys involved in the common area combination. All 35 combinations are shown. Average fluxes, standard deviation and relative errors per each survey are also detailed.

	S1	S2	S3	S4	S5	S6	S7	S8	S9	Common area (m2)
Flux Kg/(yr·m^2)			0.57	1.45	1.27	0.23		0.46	3.32	20
		0.39	0.53							6724
		0.39							2.70	15052
			0.63				1.86			16828
			0.86				0.83	5.23	1.51	148
			0.58					1.01	3.02	10568
			0.53						1.54	138064
			0.57	4.03						86816
			0.63	5.94				1.36		7744
			0.57	1.54				0.76	2.74	1608
			0.52	2.98					2.08	21992
			0.59	5.14	2.37					8628
			0.62	1.26	1.44			1.56		772
			0.57	1.45	1.27	0.23		0.46		216
			0.57	1.45	1.27	0.23			3.32	684
			0.57	1.45		0.23		0.46		216
			0.59		1.59					34656
			0.57		1.27	0.23		0.46		228
								1.54	3.23	54400
	1.16		0.58							6396
	0.84		0.59						3.74	1684
	1.18		0.58	10.70						1776
	0.85		0.59	17.63					3.74	1032
				6.34				1.91	3.63	11580
				13.09	1.39	0.64		0.51		1760
				1.44	1.35	0.35			3.42	992
		0.31					0.44			16
							0.89	0.51	0.59	21148
				9.70			5.17			18248
				10.68			2.13	1.79		6824
				5.01			0.53	1.59	3.89	1488
				6.79			0.75		3.85	4484
				3.16	2.02		0.29			412
					1.20		1.33			4444
						0.77	2.55			4264
Mean	1.00	0.35	0.59	5.77	1.50	0.36	1.52	1.30	2.86	
Stdev	0.18	0.04	0.06	4.63	0.37	0.21	1.41	1.21	0.97	
Relative error (%);	15.92	27.95	6.20	136.56	18.51	47.44	66.87	59.28	27.39	

Table SI5. Flow rates of methane for seep sites located at PKF and around the world.

Annual Flow rate (T CH_4 y^{-1})	**Water depth (m)**	**Study area**	**Reference**
1075 (850 -1300)	193-352	PKF Area 1	This study
2050 (1600 -2500)	194-410	PKF Area 2	This study
575 (450 - 700)	67-117	PKF Area 3	This study
440 -675	~240	PKF 78°38'30''-78°40'N; 9°23'- 9°28' E	Veloso et al., 2015
433 (80-1090)	240-245	PKF Area 2 (comparable to Area 1 in this article)	Sahling et al., 2014
417 (64-802)	380-390	PKF Area 3 (comparable to Area 2 in this article)	Sahling et al., 2014
304	1250–1270	Håkon Mosby Mud Volcano– all three emission sites	Sauter et al., 2006
32-1395	890	Kerch Flare, Black Sea	Römer et al, 2012a
21.9	600–700	Northern summit of Hydrate Ridge, offshore Oregon	Torres et al., 2002
24	65–75	Tommeliten field, North Sea	Schneider von Deimling et al., 2011
641.6 (±513.28)	575–2870	Makran continental margin (50 km broad segment)	Römer et al, 2012b
3.6892 to 36.892	1690	Carbonate slab, Nile Deep Sea Fan	Römer et al, 2014

Table SI6. Earthquakes event occurrences with significant magnitudes during each year (2008-2014). Magnitudes are given in the Richter scale. All earthquakes with magnitude 4 or larger are in mb units but for some of the less powerful earthquakes the magnitude is given in ML.

Year	2008	2009	2010	2011	2012	2013	2014
Count 3<M<4	11	31	20	18	8	20	12
Count M>=4	5	8	5	4	6	5	4